JOURNAL OF GEOPHYSICAL RESEARCH, VOL. 105, NO. B3, PAGES 5997-6016, MARCH 10, 2000

The chemically zoned 1949 eruption on La Palma (Canary Islands): Petrologic evolution and magma supply dynamics of a rift zone eruption

Andreas Klügel[1]

Max-Planck-Institut für Chemie, Mainz, Germany

Kaj A. Hoernle and Hans-Ulrich Schmincke

Geomar Forschungszentrum, Kiel, Germany

James D. L. White

Geology Department, University of Otago, Dunedin, New Zealand

Abstract. The 1949 rift zone eruption along the Cumbre Vieja ridge on La Palma involved three eruptive centers, 3 km spaced apart, and was chemically and mineralogically zoned. Duraznero crater erupted tephrite for 14 days and shut down upon the opening of Llano del Banco, a fissure that issued first tephrite and, after 3 days, basanite. Hoyo Negro crater opened 4 days later and erupted basanite, tephrite, and phonotephrite, while Llano del Banco continued to issue basanite. The eruption ended with Duraznero erupting basanite with abundant crustal and mantle xenoliths. The tephrites and basanites from Duraznero and Llano del Banco show narrow compositional ranges and define a bimodal suite. Each batch ascended and evolved separately without significant intermixing, as did the Hoyo Negro basanite, which formed at lower degrees of melting. The magmas fractionated clinopyroxene + olivine ± kaersutite ± Ti-magnetite at 600-800 MPa and possibly 800-1100 MPa. Abundant reversely zoned phenocrysts reflect mixing with evolved melts at mantle depths. Probably as early as 1936, Hoyo Negro basanite entered the deep rift system at 200-350 MPa. Some shallower pockets of this basanite evolved to phonotephrite through differentiation and assimilation of wall rock. A few months prior to eruption, a mixing event in the mantle may have triggered the final ascent of the magmas. Most of the erupted tephrite and basanite ascended from mantle depths within hours to days without prolonged storage in crustal reservoirs. The Cumbre Vieja rift zone differs from the rift zones of Kilauea volcano (Hawaii) in lacking a summit caldera or a summit reservoir feeding the rift system and in being smaller and less active with most of the rift magma solidifying between eruptions.

1. Introduction

Volcanic rift zones are common features of basaltic ocean island and continental volcanoes, yet a full understanding of their role in the overall magma supply system and in controlling petrologic evolution remains elusive. An exception is Kilauea volcano (Hawaii), where interdisciplinary studies have provided deeper insight into the geometry and dynamics of the volcano's magma plumbing system (see review by *Tilling and Dvorak* [1993]), yet many aspects, such as the geometry of the summit reservoir, remain controversial [*Pietruszka and Garcia*, 1999]. At Kilauea a nearly continuous supply of magma accumulates over time in a summit reservoir at 2-4 km depth, gradually inflating the summit region. Episodic lateral injection of summit magma into adjacent rift zones (a rift event) releases accumulated stress and typically, though not always, results in an eruption. Much magma is stored in the deeper part of the rift system, forming crystal mush or isolated pockets which differentiate and then either solidify or are erupted [*Wright and Fiske*, 1971; *Ryan*, 1988; *Delaney et al.*, 1990]. Mixing of distinct magmas in the summit reservoir and in the deep rift is important in controlling the composition of the erupted lavas, although some magmas bypass the summit reservoir [*Garcia et al.*, 1989, 1996].

La Palma has a well-developed active volcanic rift zone along a north-south trending ridge [*Middlemost*, 1972; *Carracedo*, 1994]. Only a few studies, however, have addressed magma transport and storage beneath and within this rift system [*Klügel et al.*, 1997] and the evolution of its magmas [*Praegel*, 1986; *Elliott*, 1991]. Here we discuss the petrology, geochemistry, and magma supply dynamics of the 1949 eruption, which serves as a case study for complex rift zone eruptions on La Palma. We show how the erupted magmas can be related to storage, fractionation, and mixing in reservoirs within the mantle and the crust and compare the situation on La Palma to that of Kilauea. The 1949 eruption is of particular interest because a variety of eruptive processes occurred during the 37 days of activity and because eyewitness accounts indicate an interconnection of widely sepa-

[1]Now at Fachbereich Geowissenschaften, Universität Bremen, Bremen, Germany.

Paper number 1999JB900334.
0148-0227/00/1999JB900334$09.00

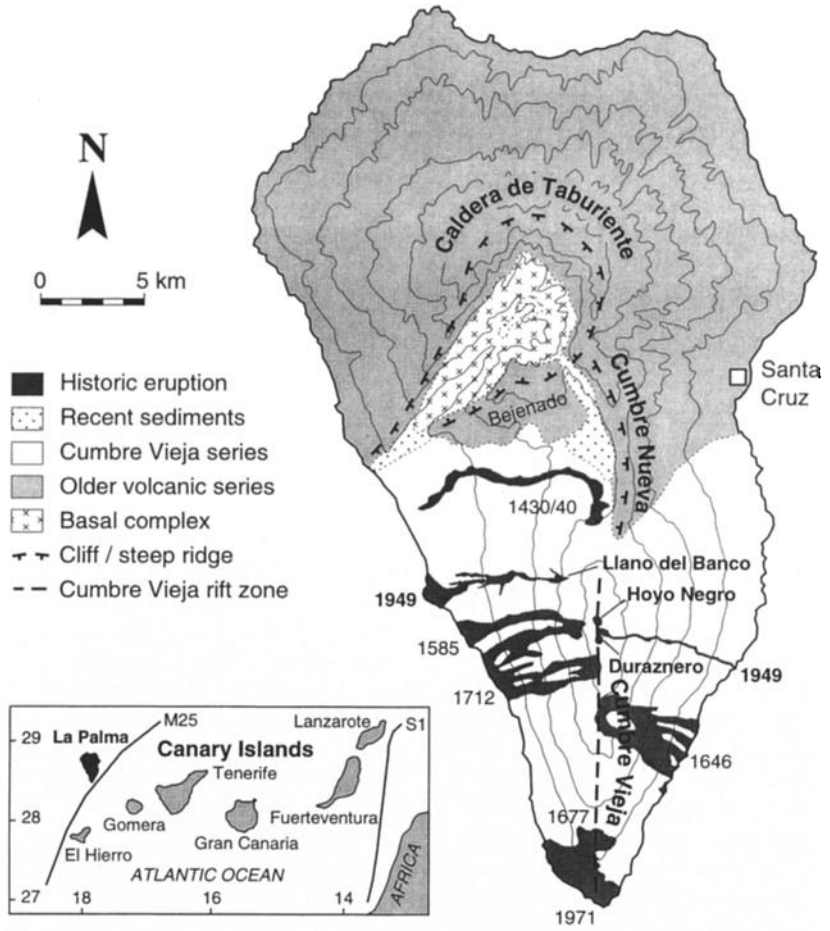

Figure 1. Location map (inset) and simplified geological map of La Palma [after *Navarro and Coello*, 1993; *Ancochea et al.*, 1994; *Carracedo et al.*, 1999]. Most historic eruptive centers are located along the north-south trending Cumbre Vieja rift zone. The three vents of the 1949 eruption are Duraznero (1880 m above sea level) and Hoyo Negro (1880 m) craters located on the Cumbre Vieja crest and Llano del Banco fissure (1300 m) at the ridge flank to the west of the rift.

rated vents. Furthermore, the late erupted lavas carry a great variety of crustal and mantle xenoliths which were studied to obtain additional information on magma ascent and storage. The 1949 eruption is also of interest because the erupted lavas show a wide range in chemical composition for a single eruption (e.g., basanite and phonotephrite were simultaneously erupted from different vents during one phase).

2. Geological Setting

The Canary Islands form a chain of seven large volcanic islands located off the northwestern African continental shelf (Figure 1). All islands are underlain by oceanic crust as indicated by tholeiitic mid-ocean ridge basalt (MORB) gabbro xenoliths occurring on Lanzarote, Gran Canaria, and La Palma [*Hoernle*, 1998; *Schmincke et al.*, 1998]. The age of the crust is bracketed by paleomagnetic anomalies S1 (175 Ma), between the easternmost islands and the African coast, and M25 (155 Ma) between La Palma and Hierro, which are the westernmost and youngest islands [*Roeser*, 1982; *Klitgord and Schouten*, 1986]. The geology of the Canary Islands is summarized by *Schmincke* [1976, 1982].

La Palma has been the most active of the Canary Islands in historic times with eruptions recorded in ~1440, 1585, 1646, 1677, 1712, 1949, and 1971 [*Hernandéz-Pacheco and Valls*, 1982]. The island consists of three main units: (1) the basal complex (3-4 Ma), which comprises a Pliocene seamount sequence and a plutonic complex that have been uplifted and tilted to their present position; (2) the older volcanic series (2 Ma to 0.7 Ma) which includes the Taburiente shield volcano, the Bejenado edifice, and the Cumbre Nueva series; and (3) the Cumbre Vieja series (0.7 Ma to present) which is confined to the southern half of the island [*Hausen*, 1969; *Middlemost*, 1972; *Abdel-Monem et al.*, 1972; *Schmincke*, 1976; *Staudigel and Schmincke*, 1984; *Ancochea et al.*, 1994; *Carracedo et al.*, 1999] (Figure 1). The north-south trending Cumbre Vieja ridge consists dominantly of mafic lava flows, cinder cones, and several phonolitic plugs. Lava compositions range from basanite to phonolite with clinopyroxene ± olivine ± kaersutitic amphibole as the major phenocryst phases. Most historic eruptions were chemically and mineralogically zoned, commonly carrying mantle and crustal xenoliths during the final eruptive phase [*Hernandéz-Pacheco and Valls*, 1982; *Ibarrola*, 1974; *Praegel*, 1986]. The Cumbre Vieja is interpreted as a volcanic rift zone because vents

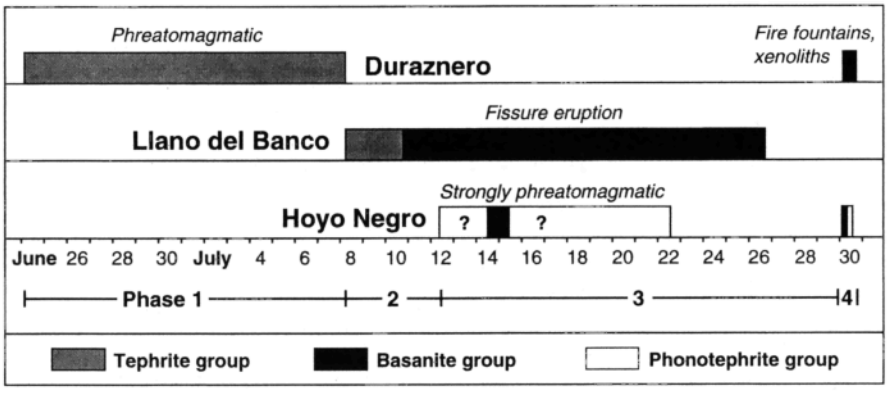

Figure 2. Chronology of the 1949 eruption. Note the bimodality of the Duraznero and Llano del Banco eruptives, the simultaneous eruption of basanite at Llano del Banco and phonotephrite at Hoyo Negro, and the synchrony of events. Hoyo Negro produced a basanitic lapilli layer during its first days of activity and basanitic bombs during the final phase, but further basanite occurrences in the eruptive sequence are uncertain. The late basanite erupted from Duraznero carried almost all xenoliths of the entire eruption.

and north-south trending fissures, faults, and dikes are concentrated along its crest [*Middlemost*, 1972; *Carracedo*, 1994].

3. Chronology of the 1949 Eruption

The short summary of the temporal evolution of the eruption given below is based on works by *Bonelli Rubio* [1950], *Romero Ortiz* [1951], and *Martel San Gil* [1960]; detailed accounts of the eruption chronology and volcanology are given elsewhere [*Klügel et al.*, 1999; *White and Schmincke*, 1999].

Seismic precursors: The first weak seismic precursors were felt south of the Caldera de Taburiente (Figure 1) from July 1936. Beginning in February 1949, strong earthquakes periodically shook the whole island almost daily. They were most intense at the southern tip of the island, causing strong ground cracking. On June 24, intense seismicity and ground cracking in the proximity of Montaña Duraznero marked the onset of the eruption.

Phase 1 (June 24 to July 8): Phreatomagmatic activity from Duraznero crater on the crest of Cumbre Vieja (1880 m above sea level (asl)). Five vents opened successively along a 400-m-long, north-south trending fissure and erupted tephritic pyroclastics.

Phase 2 (July 8-12): There was sudden opening of a fissure at Llano del Banco (1300 m asl) at the western ridge flank 3 km north of Duraznero and cessation of activity at Duraznero (Figure 2). Llano del Banco issued tephritic magma, producing a large lava flow which eventually reached the coast. Around July 10, the lava became less viscous, reflecting the arrival of basanitic magma which makes up the bulk of the erupted volume.

Phase 3 (July 12-30): Accompanied by strong seismicity, Hoyo Negro (1880 m asl) opened 500 m north of Duraznero. It erupted basanite, tephrite, and phonotephrite in violent phreatomagmatic explosions, while Llano del Banco simultaneously issued basanitic lava at rates sometimes exceeding 14 m^3/s. Eyewitness accounts indicate a close hydraulic connection between the two active vents, 2.5 km apart in distance and 580 m apart in elevation. Eventually, the activities declined and ceased entirely on July 22 (Hoyo Negro) and July 26 (Llano del Banco) (Figure 2).

Phase 4 (July 30): Explosive activity resumed at Duraznero and Hoyo Negro (Figure 2). After 3 hours, Duraznero began to erupt xenolith-rich basanite, producing lava fountains and a flow which rapidly descended toward the east coast. This final phase of the eruption terminated after 12 hours.

4. Petrography and Mineral Chemistry

On the basis of petrography and whole rock chemistry, we divide the volcanic rocks of the 1949 eruption into three groups (compare Figure 2): the tephrite group comprises tephritic pyroclastics and lavas from Duraznero and Llano del Banco (June 24 to July 10); the basanite group contains basanitic lavas and pyroclastics from Llano del Banco, Hoyo Negro, and Duraznero (July 10-30); and the phonotephrite group comprises tephritic to phonotephritic pyroclastics from Hoyo Negro (July 12-30). The Hoyo Negro pyroclastics form <1% of the total erupted volume.

4.1. Tephrite Group

Tephrites contain phenocrysts of clinopyroxene (3-5 vol %), kaersutite (1-2 vol %), Ti-magnetite (1-2 vol %), and rare plagioclase, hauyne, and olivine. The groundmass consists of glass with plagioclase laths (An_{53-56} [*Kaiser*, 1988]) and clinopyroxene and oxide microlites. Only a few, small xenoliths are present, the most common type being hauyne-bearing alkaline gabbros.

Clinopyroxenes are titaniferous augites showing a wide compositional range and variable, in many cases complex, zonation. Two principal clinopyroxene types are recognized: type 1 (Mg# = 58-66) (Mg# = molar $Mg/(Mg+Fe^{tot})x100$) is greenish and Na-rich and occurs dominantly as euhedral to anhedral cores, some of which are strongly resorbed; type 2 (Mg# = 70-80) is pale brownish and occurs as a mantle around type 1 cores, as individual phenocrysts, or as groundmass crystals (Table 1a). The green-core clinopyroxenes are reversely zoned with increasing Mg number and decreasing Na and Mn contents toward the rim. In most crystals, Ti strongly increases at the rim. Kaersutite (5-6 wt % TiO_2) is reversely or irregularly zoned with Mg# = 50-66 in partly rounded cores and Mg# = 69-71 at narrow lighter-colored rims (Table 1b). The crystals are euhedral to mildly rounded and in some cases strongly resorbed. Some kaersutites show fine-grained, polycrystalline rims or patches, indicating breakdown reactions. Rare plagioclase crystals distinct from microlites commonly show strong marginal and internal resorption ("fingerprint" textures), are partly mantled by newly grown

Table 1a. Representative Clinopyroxene Analyses (Averaged) and Calculated Pressures and Temperatures of Tephrites and Basanites

	Tephrite Samples										
	1502-1	1502-2	1502-4	1502-5	1502-7	1502-8	1502-5	1502-6	1502-7	1502-4	1502-7
Type	2,rim	2,rim	2,rim	2,rim	2,rim	2,rim	2,core	2,core	2,core	1,core	1,core
Points	4	4	3	3	3	3	6	4	1	8	4
SiO_2	44.76	43.61	42.93	46.22	46.81	45.45	44.77	47.51	45.28	44.75	41.81
TiO_2	3.90	4.55	4.57	3.49	3.12	3.79	3.21	2.54	3.01	2.74	4.02
Al_2O_3	7.67	8.65	8.95	6.79	6.19	7.19	8.08	5.25	7.80	8.13	10.18
Cr_2O_3	0.01	0.04	0.03	0.02	0.01	0.03	0.07	0.03	0.10	0.02	0.02
FeO*	7.69	8.10	8.54	7.59	7.34	7.70	7.51	7.14	7.46	9.80	11.13
MnO	0.21	0.22	0.18	0.23	0.24	0.21	0.14	0.18	0.14	0.28	0.30
MgO	11.89	11.42	11.34	12.44	12.80	12.12	12.47	13.68	12.53	10.22	8.93
CaO	22.19	22.38	22.15	22.11	22.25	21.99	21.92	22.12	22.01	21.81	21.66
Na_2O	0.71	0.74	0.69	0.68	0.61	0.74	0.64	0.55	0.63	1.00	0.97
Sum	99.0	99.7	99.4	99.6	99.4	99.2	98.9	99.1	99.0	98.8	99.1
Mg #	73.4	71.5	70.3	74.5	75.7	73.7	74.7	77.3	75.0	65.0	58.9
T, °C	1122	1119	1119	1120	1113	1119	1170	1138	1169	1052	1054
P, MPa	749	690	677	721	644	709	932	531	926	798	794
	Basanite Samples										
	1507-1	1507-2	1507-3	1507-5	1507-6	1507-7	1507-11	1507-12	1507-14	1507-1	1507-7
Type	2,rim	2,rim	2,rim	2,rim	2,rim	2,rim	2,rim	2,core	2,core	1,core	1,core
Points	4	4	4	4	4	4	4	14	5	2	10
SiO_2	45.69	45.76	47.20	46.15	45.95	48.32	47.59	46.50	46.15	43.63	47.53
TiO_2	3.41	3.15	2.63	2.67	2.86	2.31	2.35	2.36	2.69	3.20	1.52
Al_2O_3	7.07	7.50	6.18	7.17	7.50	4.85	5.79	7.18	7.01	9.38	5.32
Cr_2O_3	0.05	0.04	0.07	0.35	0.25	0.04	0.33	0.55	0.31	0.01	0.03
FeO*	7.85	7.88	7.54	7.37	7.50	7.64	7.23	6.78	8.05	9.19	11.29
MnO	0.12	0.13	0.15	0.12	0.11	0.16	0.13	0.12	0.13	0.23	0.49
MgO	12.28	12.42	13.34	12.93	12.73	13.90	13.58	13.38	13.28	10.19	9.96
CaO	22.38	21.96	22.07	22.17	22.30	21.93	22.03	22.06	21.70	21.68	21.60
Na_2O	0.53	0.58	0.48	0.50	0.53	0.44	0.46	0.52	0.49	0.94	1.27
Sum	99.4	99.4	99.7	99.4	99.7	99.6	99.5	99.5	99.9	98.7	99.1
Mg #	73.6	73.8	75.9	75.8	75.2	76.4	77.0	77.9	74.6	66.4	61.1
T, °C	1134	1141	1130	1132	1136	1116	1126	1223	1220	1052	1047
P, MPa	691	766	624	652	695	443	583	1090	1040	769	756

Mg # = molar $Mg/(Mg+Fe^{tot})x100$. See text for details of the thermobarometric calculations.

plagioclase, and are interpreted as xenocrysts. Olivine occurs as rare xenocrysts in schlieren and in a few hybrid samples compositionally between tephrites and basanites.

4.2. Basanite Group

The basanites can be subdivided geochemically into the Llano del Banco, Duraznero, and Hoyo Negro subgroups, as shown in section 7.1. Basanites contain phenocrysts of clinopyroxene (7-10 vol %), olivine (3-5 vol %), and minor Ti-magnetite. The groundmass consists of glass with plagioclase laths (An_{60-67}) and clinopyroxene, olivine, and oxide microlites. Partly resorbed crystals or glomerocrysts of plagioclase, amphibole, and large clinopyroxene (>2 mm) are interpreted as disaggregated wall rock or xenoliths.

Clinopyroxenes are titaniferous augites petrographically resembling those in tephrites. Similarly, greenish type 1 (Mg # = 60-66) and brownish type 2 (Mg # = 74-83) clinopyroxenes can be distinguished, which differ from those in tephrites in having lower Ti and Al and higher Cr contents, as well as a slightly higher Mg number (Table 1a). Many crystals, including reversely zoned green-core clinopyroxenes, show a decrease of Mg number and Cr at the outermost rim (<20 μm); some clinopyroxenes show complex zonation. Olivine occurs in two varieties: type 1 is normally zoned, having a core composition of Fo_{84} followed by a steep decrease to Fo_{73-76} at the rim (20-90 μm); type 2 is larger than type 1 and shows a gradual change from Fo_{80} in the core toward Fo_{84} maximum (60-300 μm) followed by a steep normal zonation to Fo_{73-76} at the rim (Figure 3). Most olivines are euhedral, and some contain spinel inclusions.

Table 1b. Representative Amphibole Analyses of 1949 Tephrite

	Sample			
	1502-1	1502-1	1502-3	1502-3
Type	rim	core	rim	core
SiO_2	39.03	38.42	38.95	39.06
TiO_2	5.33	5.55	5.77	6.07
Al_2O_3	13.75	14.15	13.81	13.56
FeO*	10.54	12.93	10.25	11.26
MnO	0.19	0.16	0.07	0.19
MgO	13.66	11.86	13.46	12.24
CaO	12.61	12.42	12.56	12.68
Na_2O	2.35	2.40	2.31	2.45
K_2O	1.04	1.16	1.16	1.17
P_2O_5	0.15	0.10	0.13	0.15
F	0.19	0.14	0.18	0.15
Cl	0.03	0.02	0.02	0.01
Sum	98.9	99.3	98.6	99.0
Mg #	69.8	62.1	70.1	66.0

4.3. Phonotephrite Group

This group comprises phonotephrites to tephrites from Hoyo Negro containing phenocrysts of amphibole (3-8 vol %), clinopyroxene (2-5 vol %), minor oxides, and rare apatite. The groundmass consists of abundant plagioclase laths, clinopyroxene, oxides, and glass. Most phenocrysts are strongly zoned, with green-core clinopyroxenes and kaersutites with light colored rims being particularly common. Many have corroded cores with apatite, titanite, or hauyne inclusions resembling those in mafic and ultramafic xenoliths. Fine-grained, oxide-rich reaction rims around kaersutites, in a few cases newly overgrown, are the rule in many phonotephrites but are nearly absent in others. Some kaersutites show sieve-like resorption textures. Practically all rocks contain dark schlieren (up to 50 vol %) and small (<5 mm) angular xenoliths and xenocrysts including olivine, titanite, apatite, and hauyne. Remarkably, the phonotephrites only contain fragments of mafic and ultramafic cumulates but not of tholeiitic gabbros, in contrast to the xenolith abundances in the late Duraznero basanite (see section 4.4).

4.4. Xenoliths

Over 99% of the xenoliths of the 1949 eruption occur in the terminal Duraznero basanite where they make up almost 1 vol % [*Klügel et al.*, 1999]. The xenolith suite consists of (1) tholeiitic gabbros (40% relative abundance) representing fragments of the Jurassic oceanic crust [*Hoernle*, 1998; *Schmincke et al.*, 1998]; (2) alkaline hauyne- and titanite-bearing gabbros (35%) with cumulus textures, interpreted as fragments of crustal intrusions; (3) olivine-bearing pyroxenites and kaersutitites (20%), interpreted as cumulates from mafic alkaline magmas rising beneath La Palma, which may have formed at both mantle and crustal depths [*Hansteen et al.*, 1998]; (4) basanitic fragments (5%), resembling fragments of dikes or lava flows now buried at depth; (5) at least five types of felsic, strongly fused xenoliths (<1%) with syenitic, phonolitic and rhyolitic compositions, interpreted as crustal fragments from various depths; and (6) spinel dunites and harzburgites (<<1%) from the upper mantle [*Klügel*, 1998].

5. Thermobarometry

5.1. Redox State and Oxygen Fugacity

The bulk rock Fe_2O_3/FeO ratios of nine basanites as determined by FeO titration range from 0.34 to 0.69 (average 0.47) overlapping with results from previous wet chemical analyses (0.30 to 0.55, average 0.38) [*Hernandéz-Pacheco and Valls*, 1982]. We calculated the oxygen fugacity (f_{O2}) from the redox state using the equation of *Carmichael and Ghiorso* [1990] for glassy lava at atmospheric pressure. Fe_2O_3/FeO ratios from 0.30 to 0.69 yield fugacities of 0.8 to 2.6 log unit above the QFM buffer for the bulk basanite. Since the magmas have undoubtedly been oxidized during ascent and eruption, we consider $Fe_2O_3/FeO = 0.30$ and f_{O2} = QFM+0.8 (e.g., 10^{-9} bars at 1100°C) as the best approximation for the intratelluric magma. The redox state of the 1949 tephrite is within the range for the basanite [*Hernandéz-Pacheco and Valls*, 1982] yielding a similar oxygen fugacity (QFM+1).

5.2. Tephrite Thermobarometry

According to the relation of *Duke* [1976], clinopyroxene coexisting with the tephrite melt or the bulk rock (Tables 2 and 3) has Mg # = 73 and Mg # = 76, respectively, which is within the range for brownish type 2 clinopyroxenes. Applying the clinopyroxene-melt thermobarometer of *Putirka et al.* [1995] to clinopyroxene rim and melt compositions yields 1110-1120°C and 640-750 MPa (N=6). If appropriate type 2 clinopyroxene cores (Mg # = 75-78) are related to the bulk rock composition, we obtain 1160-1170°C and 840-930 MPa (N=4) with two crystals falling outside this range (530 and 640 MPa) (Table 1a and Figure 4).

Greenish clinopyroxenes (type 1) are xenocrystic to the tephrite because of their low Mg # (58-66). If the relation of *Duke* [1976] holds for evolved compositions, then this melt may have had a Mg # of 22-29, which only matches phonolite among recent La Palma rocks. Thus, to bracket the crystallization depth of greenish clinopyroxenes, we assigned a representative phonolite composition (Table 3) for the *Putirka et al.* [1995] thermobarometer. This yielded 750-820 MPa (N=5) which adjoins the range for brownish clinopyroxene rims. On the basis of their Mg number, green-core clinopyroxenes may have coexisted with reversely zoned kaersutites following the relation of *Irving and Price* [1981].

5.3. Basanite Thermobarometry

Following *Duke* [1976], clinopyroxene coexisting with the basanite melt or the bulk rock (Tables 2 and 3) has Mg # = 73 and Mg # = 81, respectively. Most brownish clinopyroxene rims (type 2) have Mg # = 73-76 and appear to be in equilibrium with the melt. The thermobarometer of *Putirka et al.* [1995] indicates 1120-1140°C and 580-770 MPa (N=13); one phenocryst yields 440 MPa. If the most magnesian clinopyroxene cores can be related to the bulk rock composition, then we obtain 1200-1220°C and 910-1110 MPa (N=6) as first-order estimates. Greenish type 1 clinopyroxenes, by analogy with the tephrite, are xenocrystic and are interpreted to have grown in a phonolitic melt possibly at pressures of 740-830 MPa (N=5) (Table 1a and Figure 4).

Using a melt Fe_2O_3/FeO ratio of 0.30, the partition coefficient of *Roeder and Emslie* [1970] indicates Fo_{74} for olivine coexisting with the basanite melt and Fo_{83} for the bulk rock (Tables 2 and 3), which corresponds well with the phenocryst rim and core compositions, respectively (Figure 3). Olivine-melt thermometers with corrections for melt composition and pressure [*Putirka*, 1997; *Ford et al.*, 1983] indicate 1110-1130°C for the melt and 1190-1230°C for the bulk rock at atmospheric pressure, and ~5°C higher temperatures for each 100-MPa pressure increase (Figure 4). The temperatures obtained for clinopyroxene and olivine thus correspond well with each other. According to *Duke* [1976] and *Irving and Price* [1981], however, even the most magnesian clinopyroxenes were probably not in equilibrium with Fo_{84} olivine (type 1 cores) but possibly with Fo_{80} (type 2), as has also been noted for the 1971 eruption on La Palma [*Praegel*, 1986].

There is a good overlap of the calculated pressures for tephrite and basanite, suggesting that both fractionated at ~600-800 MPa and possibly at higher pressures. This is in accordance with clinopyroxene preceding plagioclase as the fractionating phase [*Fisk et al.*, 1988]. The data are supported by CO_2-dominated fluid inclusions in phenocrysts of the basanite showing a bimodal density distribution: Minimum pressures of inclusion entrapment are 600-680 MPa (upper mantle) for olivine and 200-340 MPa

[1]Supporting data tables are available on diskette or via Anonymous FTP from kosmos.agu.org, directory APEND (Username = anonymous, Password = guest). Diskette may be ordered from American Geophysical Union, 200 Florida Avenue, N.W., Washington, DC 20009 or by phone at 800-966-2481; $15.00. Payment must accompany order.

Table 3. XRF Whole Rock Data of Representative 1949 Samples

	Analysis													
	1	2	3	4	5	6	7	8	9	10	11	12	13	14
Locality	Dur	Dur	Dur	Dur	Dur	LdB	LdB	LdB	LdB	HN	HN	HN	HN	HN
Rock type	T	T	T/B	B	B	T	T	B	B	B	B	B	PT-A	PT-A
SiO_2	45.43	45.22	44.73	43.41	43.76	45.29	45.31	44.06	43.95	44.12	42.42	43.54	48.75	48.67
TiO_2	3.41	3.39	3.39	3.46	3.42	3.39	3.36	3.39	3.53	3.48	3.40	3.62	2.52	2.59
Al_2O_3	16.27	16.05	15.01	13.64	13.70	16.08	16.07	13.76	14.40	13.91	11.77	12.82	17.60	17.06
Fe_2O_3	11.89	11.65	12.42	13.62	13.70	11.65	11.50	13.61	13.26	13.80	13.57	13.44	9.43	9.59
MnO	0.21	0.21	0.21	0.20	0.20	0.21	0.21	0.20	0.20	0.20	0.19	0.21	0.21	0.21
MgO	4.93	4.91	6.40	7.97	8.18	4.96	4.90	8.23	7.36	8.03	11.76	9.84	3.37	4.04
CaO	9.17	9.09	9.76	10.63	10.69	9.12	9.02	10.53	10.14	10.85	10.64	10.97	7.14	7.14
Na_2O	5.08	5.24	4.68	3.76	3.76	5.48	5.46	3.77	3.89	3.64	3.06	3.29	5.73	5.75
K_2O	2.29	2.32	1.89	1.26	1.28	2.31	2.36	1.32	1.53	1.31	1.39	1.42	2.88	2.92
P_2O_5	0.90	0.87	0.81	0.72	0.70	0.85	0.89	0.69	0.75	0.69	0.69	0.84	0.76	0.74
SO_3	0.08	<LLD	<LLD	0.08	<LLD	<LLD	<LLD	<LLD	<LLD	0.09	<LLD	<LLD	0.06	0.12
H_2O+CO_2	0.47	0.42	0.27	0.26	0.26	0.22	0.32	0.20	0.75	0.30	0.53	0.30	0.43	0.42
Total	100.1	99.4	99.6	99.0	99.7	99.6	99.4	99.8	99.8	100.4	99.4	100.3	98.9	99.2
Mg #	45.1	45.5	50.5	53.7	54.2	45.8	45.8	54.5	52.4	53.6	63.2	59.2	41.5	45.5
V	262	257	273	298	299	254	237	280	294	309	305	290	182	191
Cr	36	47	161	309	338	48	46	328	237	328	767	377	39	60
Co	57	34	40	61	49	30	28	58	55	46	60	62	39	23
Ni	46	50	86	133	142	44	46	135	118	126	309	215	35	53
Cu	65	70	80	101	108	59	63	102	96	89	116	113	56	58
Zn	137	130	125	127	126	127	129	119	129	143	116	126	134	141
Ga	27	24	22	19	21	22	23	19	22	19	16	21	30	29
Rb	65.38*	67.77*	44	33.51*	29	66.18*	68.91*	31.39*	33	30	37.79*	33	69	103.2*
Sr	1425	1426	1211	932	979	1373	1446	932	1073	975	916	1205	1856	1791
Y	44.59*	44.10*	39	38.10*	35	42.92*	44.39*	33.85*	35	34	32.81*	36	42	43.65*
Zr	427	445	370	273	290	415	443	280	318	284	273	344	570	640
Nb	119	115	101	62	68	107	121	67	77	74	70	96	168	193
Ba	786	768	622	435	452	752	790	427	498	482	500	597	1169	1095
La	108.6*	109.1*	94	66.85*	70	106.2*	109.4*	64.35*	79	65	68.02*	96	178	154.9*
Ce	198.6*	201.0*	162	131.3*	129	194.7*	200.6*	126.5*	133	135	128.4*	173	263	257.1*
Pr	22.15*	22.22*	15	15.60*	15	21.79*	22.22*	14.83*	14	15	14.66*	19	25	25.99*
Nd	80.20*	80.52*	68	60.29*	57	79.10*	81.16*	57.18*	62	61	55.23*	74	86	86.11*
Sm	14.11*	13.87*	14	11.33*	12	13.88*	14.18*	10.73*	6	11	10.19*	13	14	13.62*
Eu	4.13*	4.09*	-	3.41*	-	4.04*	4.08*	3.25*	-	-	3.02*	-	-	3.88*
Gd	11.94*	11.97*	-	9.92*	-	11.55*	11.86*	9.49*	-	-	8.81*	-	-	11.41*
Tb	1.55*	1.53*	-	1.33*	-	1.52*	1.53*	1.27*	-	-	1.18*	-	-	1.47*
Dy	7.67*	7.62*	-	6.74*	-	7.45*	7.55*	6.41*	-	-	5.90*	-	-	7.22*
Ho	1.38*	1.37*	-	1.19*	-	1.35*	1.34*	1.14*	-	-	1.04*	-	-	1.30*
Er	3.50*	3.51*	-	2.98*	-	3.44*	3.48*	2.87*	-	-	2.66*	-	-	3.48*
Tm	0.44*	0.44*	-	0.36*	-	0.44*	0.44*	0.36*	-	-	0.33*	-	-	0.45*
Yb	2.77*	2.70*	-	2.22*	-	2.70*	2.71*	2.19*	-	-	2.05*	-	-	2.87*
Lu	0.38*	0.37*	-	0.31*	-	0.37*	0.38*	0.30*	-	-	0.28*	-	-	0.41*
Hf	9.17*	9.34*	-	6.79*	-	9.21*	9.14*	6.66*	-	-	6.27*	-	-	11.73*
Ta	6.13*	6.19*	-	4.10*	-	6.04*	6.19*	3.92*	-	-	3.97*	-	-	9.58*
Pb	5.95*	5.82*	-	3.90*	-	5.94*	6.15*	3.51*	-	-	2.99*	-	-	2.81*
Th	12.65*	12.62*	-	6.45*	-	12.40*	12.56*	6.11*	-	-	7.42*	-	-	26.80*
U	3.55*	3.49*	-	1.73*	-	3.48*	3.54*	1.69*	-	-	1.91*	-	-	9.61*

Major elements in weight percent; trace elements in ppm. Trace element data of selected samples analyzed by ICP-MS are indicated by asterisk. B, basanite; T, tephrite; PT, phonotephrite; Phon, phonolite; Dur, Duraznero; LdB, Llano del Banco; HN, Hoyo Negro; LLD, lower limit of detection, Mg # = molar $Mg/(Mg+Fe^{tot})x100$.

Samples in analyses are as follows: 1, KLA1502, scoriaceous layer between lithics at southern Dur crater rim; 2, KLA1519, chilled bomb 150 m SW of Dur crater; 3, KLA1521, welded spatter 100 m west of Dur crater; 4, KLA1507, late scoriaceous lapilli fallout around Dur crater; 5, WHJ9224, lava from late Dur flow; 6, KLA1203, glassy crust of early LdB lava at 1100 m asl; 7, KLA1215, early LdB lava at 1270 m asl; 8, KLA1210, terminal aa lava from LdB; 9, KLA1213, scoriaceous lapilli near LdB vent; 10, KLA1508, scoriaceous lapilli layer within HN fallout 500 m NNW of crater; 11, KLA1513, chilled bomb 150 m NW of HN crater; 12, KLA1516, chilled bomb at HN crater rim; 13, KLA1512, cauliflower bomb 150 m NW of HN crater; 14, KLA1514, late bomb 150 m NW of HN crater; 15, WHJ9254, breadcrust bomb from ridge north of HN; 16, KLA1509, bomb 100 m west of HN crater; 17, HUS251921, quenched bomb 200 m NNW of HN crater; 18, KLA1517, chilled bomb at HN crater rim; 19, KLA1624, pahoehoe lava from 1712 eruption; 20, KLA1613, prehistoric phonolite dome near Jedey village.

Table 3. (continued)

	Analysis					
	15	16	17	18	19	20
Locality	HN	HN	HN	HN	1712	prehist.
Rock type	PT-A	PT-B	PT-B	PT-B	B	Phon.
SiO_2	47.14	46.03	45.38	45.41	42.60	54.36
TiO_2	3.13	3.16	3.09	3.52	3.88	1.12
Al_2O_3	15.76	17.08	16.13	15.32	12.74	20.21
Fe_2O_3	11.18	10.32	10.77	12.08	13.84	4.75
MnO	0.21	0.24	0.24	0.23	0.20	0.17
MgO	5.51	3.30	3.57	6.18	8.81	0.86
CaO	8.50	8.84	8.89	9.01	11.52	3.91
Na_2O	5.19	6.01	6.07	4.89	3.60	8.42
K_2O	2.49	2.70	2.69	2.38	1.62	4.18
P_2O_5	0.83	1.07	1.14	0.89	0.89	0.23
SO_3	0.06	<LLD	<LLD	0.11	<LLD	0.35
H_2O+CO_2	0.36	0.27	0.31	0.42	0.39	0.23
Total	100.4	99.0	98.3	100.4	100.1	98.8
Mg #	49.4	38.8	39.6	50.3	55.8	26.4
V	221	219	209	257	327	80
Cr	115	<LLD	21	127	349	<LLD
Co	39	22	16	51	54	12
Ni	77	8	15	84	150	6
Cu	60	27	35	71	115	15
Zn	137	131	142	141	121	111
Ga	26	21	25	26	18	30
Rb	70	78.87*	78.63*	58	37	122
Sr	1572	1594	1892	1618	1194	1510
Y	37	51.28*	40.89*	43	36	24
Zr	549	453	614	495	310	630
Nb	164	122	185	150	87	118
Ba	940	865	1034	849	612	1165
La	155	134.2*	145.1*	138	99	127
Ce	238	244.5*	264.8*	240	157	173
Pr	24	26.94*	31.19*	25	19	22
Nd	84	96.57*	111.9*	87	65	47
Sm	12	16.40*	18.62*	15	12	<LLD
Eu	-	4.68*	5.05*	-	-	-
Gd	-	13.60*	13.73*	-	-	-
Tb	-	1.75*	1.90*	-	-	-
Dy	-	8.74*	9.58*	-	-	-
Ho	-	1.58*	1.69*	-	-	-
Er	-	4.10*	4.48*	-	-	-
Tm	-	0.53*	0.58*	-	-	-
Yb	-	3.30*	3.68*	-	-	-
Lu	-	0.45*	0.53*	-	-	-
Hf	-	9.86*	13.24*	-	-	-
Ta	-	7.02*	9.33*	-	-	-
Pb	-	7.87*	9.46*	-	-	-
Th	-	16.63*	18.44*	-	-	-
U	-	4.21*	5.23*	-	-	-

(lower crust) for clinopyroxene (Figure 4), which is interpreted to reflect two levels of magma stagnation during ascent [*Hansteen et al.*, 1998]. The range for olivine thus overlaps completely with that obtained by clinopyroxene-melt barometry, whereas the range for clinopyroxene overlaps with that for fluid inclusions in various xenoliths in the 1949 basanite [*Hansteen et al.*, 1998]. The data suggest that the clinopyroxene-melt barometer and olivine fluid inclusions could preserve mantle pressures because magma stagnation at crustal levels was too short for re-equilibration.

6. Zoning and Reaction Rates of Phenocrysts

6.1. Olivine Phenocryst Zonations

In order to assess the magma ascent dynamics of the 1949 eruption we used diffusion kinetics to model the zonations of olivine phenocrysts. Because the effects of simultaneous crystal growth cannot be quantified precisely, we neglect them and only calculate diffusion times to constrain an upper limit for the actual time to produce the zonations. We focus on Fe-Mg interdiffusion in olivine because it is well known and little affected by simultaneous diffusion of trace elements [*Chakraborty*, 1997] using a diffusion coefficient D_{FeMg} of 1.3×10^{-16} m^2 s^{-1} (see Appendix B).

Normal Fe-Mg zonations of olivine phenocrysts toward the rims are typically 20-90 μm wide, with some of this variation reflecting oblique cutting in thin section and anisotropy of diffusivity. Calculated diffusion times range from 2 to 45 days (see Appendix B). Although Fe, Mg, Ni, and Ca have distinct diffusivities, their zonation widths are similar (Figure 3), and we conclude that crystal growth dominated over diffusion and that the rims grew within a few days at most. The similarity of zonations during 3 weeks of eruption and their rapid growth suggest that they were not caused by intratelluric cooling of the basanite or mixing with a more evolved melt. The zonations most likely reflect crystal nucleation and growth resulting from degassing and undercooling of rapidly ascending basanite [*Sparks and Pinkerton*, 1978].

Reverse Fe-Mg zonations of type 2 olivines between their cores and maxima (Figure 3) are 60-300 μm wide. Calculated diffusion times range from 19 to 480 days using a simplified

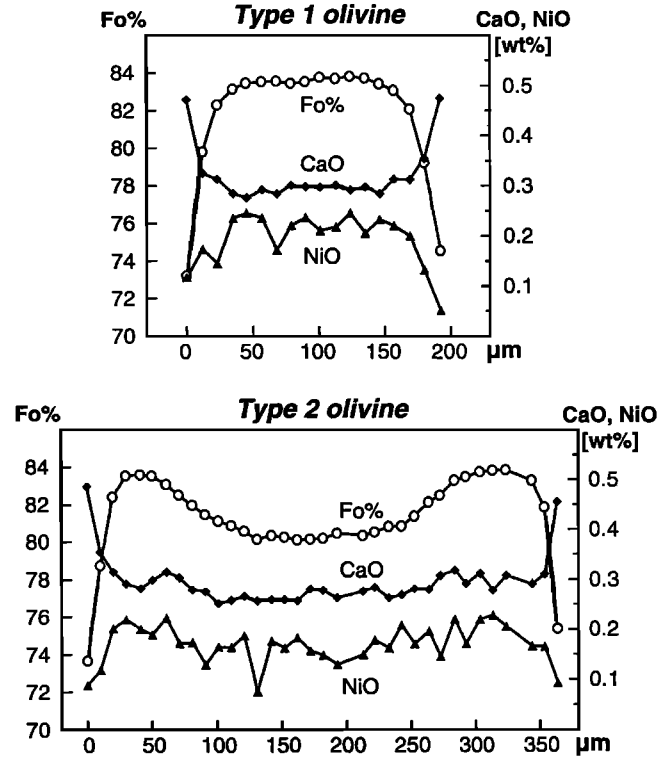

Figure 3. Microprobe traverses through representative type 1 and type 2 olivine phenocrysts in basanite. Note the similar compositions of type 1 cores and type 2 maxima and their similar rim zonations and compositions.

Table 2. Electron Microprobe Analyses of Basanite and Tephrite Glasses Used for Thermobarometric Calculations

	Tephrite KLA1502		Basanite KLA1507	
	Mean	σ	Mean	σ
SiO_2	50.11	0.28	44.91	0.20
TiO_2	2.57	0.14	4.02	0.13
Al_2O_3	18.85	0.16	15.24	0.12
FeO*	7.43	0.18	11.76	0.13
MnO	0.22	0.05	0.22	0.05
MgO	2.76	0.07	4.32	0.06
CaO	6.21	0.16	9.75	0.08
Na_2O	6.68	0.08	4.94	0.05
K_2O	3.45	0.09	1.90	0.05
P_2O_5	1.07	0.05	1.18	0.04
SO_2	0.05	0.03	0.09	0.04
F	0.24	0.04	0.22	0.05
Cl	0.14	0.02	0.06	0.02
Total	99.8	0.4	98.6	0.3
mg#	39.8	0.7	39.7	0.5

In weight percent. For tephrite N=55 and for basanite N=29, where N is number of analyses.

diffusion model (see Appendix B). On the basis of the above arguments, we conclude that the zonations formed during a significantly shorter period of a few weeks to months. The reverse zonations of type 2 olivines imply an increase of the Mg/Fe^{2+} ratio of the host melt, which most likely reflects mixing with a more primitive melt.

6.2. Amphibole Breakdown

Fine-grained, oxide-rich rims around kaersutite in some tephrites and most phonotephrites and the lack of such rims along cleavage cracks indicate amphibole breakdown resulting from reaction with the melt which reduced its dissolved water content during ascent, rather than from surface oxidation. The width of most reaction rims is ~10-40 μm in phonotephrites and up to 10 μm in tephrites. Experiments with dacitic magma show that reaction rims of similar thickness form within days to weeks once amphibole becomes unstable due to decompression and melt degassing [*Rutherford and Hill*, 1993]. Other conditions being equal, the reaction rates increase with increasing temperature and decreasing melt viscosity (M. Rutherford, personal communication, 1998). Although these experiments cannot be directly applied to kaersutite breakdown in tephrites and phonotephrites, the results provide a rough estimate for the timescale involved. We thus propose that the observed reaction rims formed within days to weeks once kaersutite became unstable due to magma degassing.

7. Major and Trace Element Chemistry

7.1. Composition of Eruptive Products

The volcanic rocks from the 1949 eruption show a wide range in chemical composition (Table 3), but most are within the range of other recent Cumbre Vieja lavas. Llano del Banco and Duraznero each produced lava flows and pyroclastics with similar but essentially bimodal chemical compositions (Figures 5 and 6). Both erupted tephrites (4.8-6.5 wt % MgO, 44.8-46.3 wt % SiO_2) and basanites (7.4-8.3 wt % MgO, 44.0-44.7 wt % SiO_2) each defining a narrow compositional range. Dark schlieren and olivine crystals in some tephrites reflect minor mixing during the transition from tephrite to basanite eruption. When plotted as a time series, however, the tephrites and basanites show gradual variations of trace element concentrations indicating a chemical zonation of the magmas (Figure 7). This is particularly striking for the basanite K_2O/P_2O_5, Rb/Ba, and Zr/La ratios which are not fractionated by the observed phenocryst phases. The data indicate subtle but systematic geochemical differences between the basanites from the three eruptive centers of 1949: from Llano del Banco to Duraznero to Hoyo Negro, the concentrations of incompatible and some compatible elements increase and ratios such as K_2O/P_2O_5, Rb/Ba, and Zr/La decrease slightly (Figure 6). The basanites from Hoyo Negro show larger compositional heterogeneities which partly reflect phenocryst accumulation (e.g., ~25 vol % olivine and clinopyroxene cause high MgO, Ni, and Cr of sample KLA1513).

The phonotephrite group of Hoyo Negro is compositionally heterogeneous and forms two distinct subgroups: Phonotephrite A follows the compositional path defined by other recent Cumbre Vieja rocks, albeit at higher concentrations of some compatible and incompatible trace elements (e.g., Cr, Ni, Zr, La), whereas phonotephrite B diverges from this path extending to lower MgO and Ni and to higher concentrations of incompatible elements at similar SiO_2 contents (Figures 5 and 6). There is also a tendency for kaersutite breakdown reactions to be more common and intense in phonotephrite A than in phonotephrite B samples. Some phonotephrites have trace element concentrations similar to far more evolved Cumbre Vieja rocks: For example, our unpublished data from eight phonolites range from 562 to 872 ppm for Zr (660, maxima for Hoyo Negro), 110 to 204 ppm for Nb (203), and 101 to 149 ppm for La (179). It is most remarkable that Hoyo Negro erupted some of the most mafic as well as the most evolved magmas of the entire eruption, providing the highest and the lowest concentrations of most major and trace elements.

Overall, from basanites to phonotephrites, Th/U decreases systematically from 3.9 to 2.8, Rb/Ba increases from 0.05 to 0.10, and La/Sm increases from 5.7 to 11.4, whereas Sm/Yb remains constant at 5.0 ± 0.2. With few exceptions, samples of the phonotephrite group have Zr/Nb ratios of 3.3 ± 0.1 clearly below those for the tephrite and basanite groups. All 1949 magmas are strongly enriched in the light relative to the heavy rare earth elements (REE), showing mildly concave upward shaped spectra without notable anomalies (Figure 8a). Low Rb/Nb, Ba/Nb and Ba/La ratios and troughs for K and Ti in normalized incompatible element patterns (Figure 8b) are consistent with derivation of the magmas from a HIMU-type source [*Weaver*, 1991] (HIMU = high $^{238}U/^{204}Pb$).

Much of the major and trace element variation of the 1949 and other Cumbre Vieja lavas is consistent with removal of olivine, clinopyroxene, kaersutite, and minor Ti-magnetite, which are the major phenocryst phases and also the major constituents (>98 vol %) of ultramafic cumulate xenoliths abundant on La Palma. The low MgO, Ni, and Cr concentrations of even the most primitive rocks indicate that the magmas have undergone significant fractionation of olivine and clinopyroxene. Clinopyroxene phenocrysts were fractionated over the entire compositional range, causing a decrease in CaO, CaO/Al_2O_3, and Cr from basanites to phonotephrites (Figure 6). Kaersutite becomes a major fractionating phase above ~45 wt % SiO_2 as indicated by minor kinks for Na_2O/K_2O and TiO_2 in Figure 6, where the latter also reflects removal of Ti-magnetite. The fractionation of both

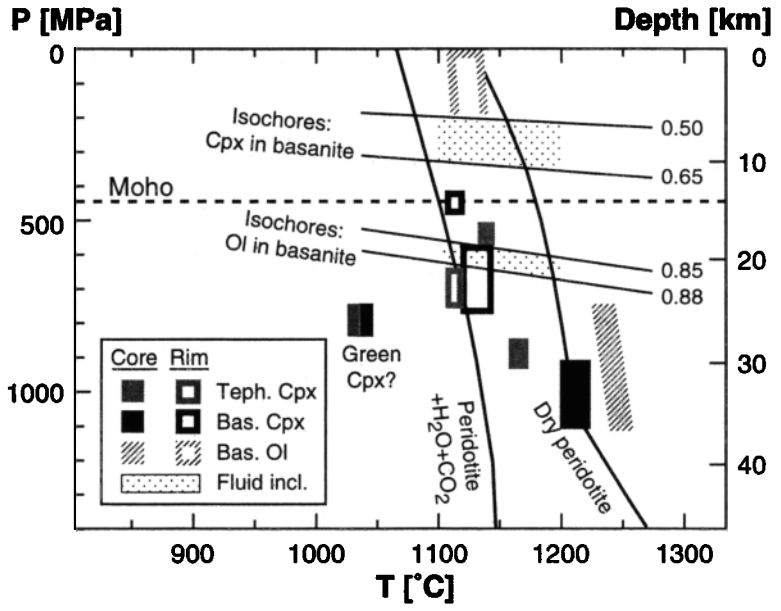

Figure 4. P-T-diagram showing thermobarometric data for magmas and xenoliths of the 1949 eruption (Cpx, clinopyroxene-melt thermobarometer; Ol, olivine-melt thermometer; Teph, tephrite; Bas, basanite). Mineral thermobarometers were applied to phenocryst rim + melt (open symbols) and phenocryst core + whole rock (solid symbols) compositions. Fluid inclusion data for basanite phenocrysts (dotted) are from *Hansteen et al.* [1998]; numbers on isochores indicate inclusion density in g cm^{-3}. The depth of the Moho is after *Ranero et al.* [1995]. Thick lines are solidi for peridotite + CO_2 + H_2O [*Olafsson and Eggler*, 1983] and dry peridotite [*Takahashi and Kushiro*, 1983].

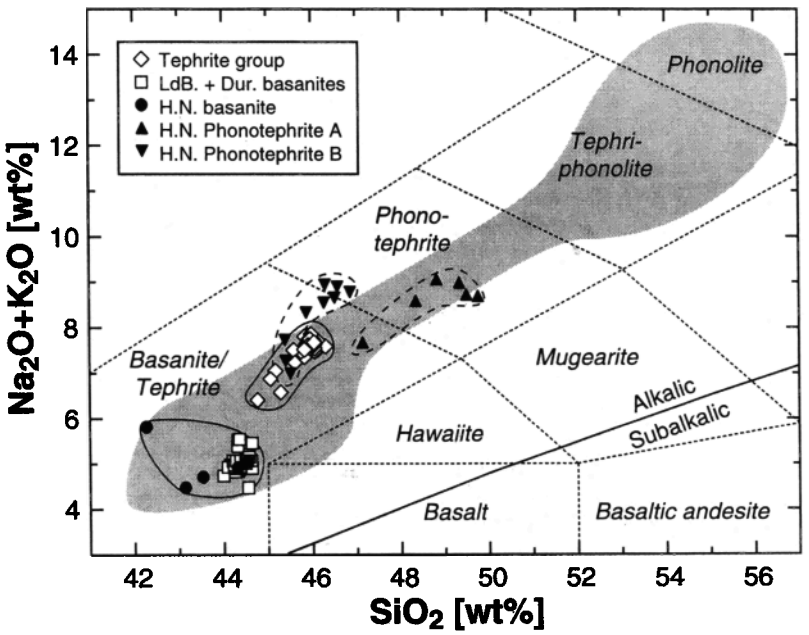

Figure 5. Total alkalis versus silica (TAS) diagram with field boundaries from *Le Maitre et al.* [1989] showing the compositional range of the 1949 eruptives as compared to other recent lavas and intrusions of the Cumbre Vieja ridge (shaded field; data from *Hernandéz-Pacheco and Valls* [1982], *Hernandéz-Pacheco and De la Nuez* [1983], *Elliott* [1991], and our unpublished data, 1999). The tephrites from Llano del Banco (LdB) and Duraznero (Dur) show complete overlap and therefore are denoted with the same symbol. Note the pronounced bimodality of the tephrite and basanite groups (fields with solid lines, 77 samples), the small compositional range of both groups, and the wide compositional range of the phonotephrite group (fields with dashed lines, 15 samples) from Hoyo Negro (HN).

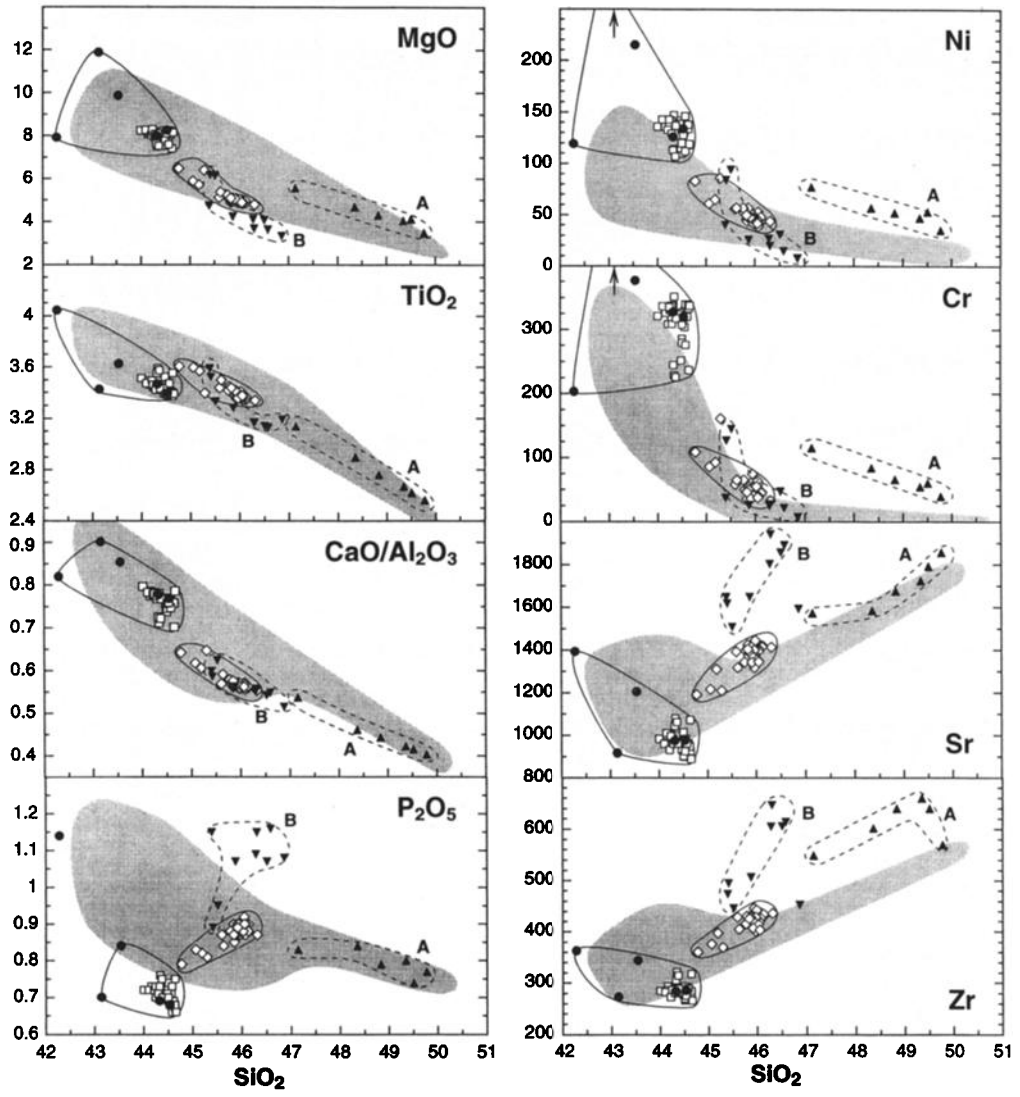

Figure 6a. Variation diagrams of the 1949 eruptives and other recent Cumbre Vieja lavas (symbols and data sources as in Figure 5). The tephrite and basanite groups are enclosed with solid lines, and Hoyo Negro phonotephrites A and B are enclosed with dashed lines. Error bars show 2σ analytical precision and are omitted where smaller than symbol size. Concentrations are in weight percent for oxides and parts per million for elements. The Harker diagrams show distinct fields for tephrites and basanites, with few samples of intermediate composition, and well-defined phonotephrite subgroups (A and B) of Hoyo Negro. Arrows indicate high Cr and Ni contents of sample KLA1513 being outside the plot range.

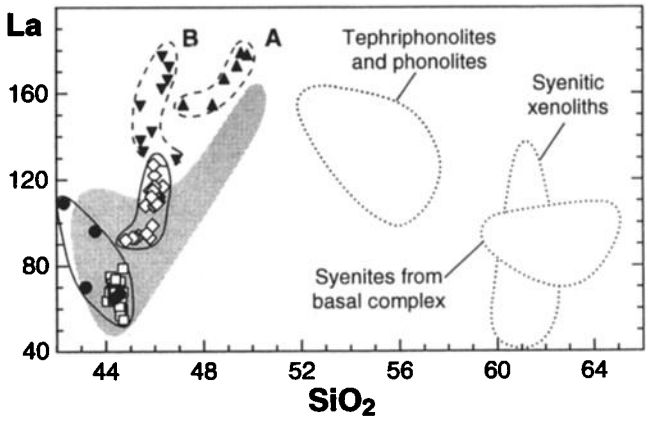

Figure 6b. Plot of La versus SiO_2 indicating the high concentrations of incompatible elements in Hoyo Negro phonotephrites as compared to highly evolved La Palma rocks.

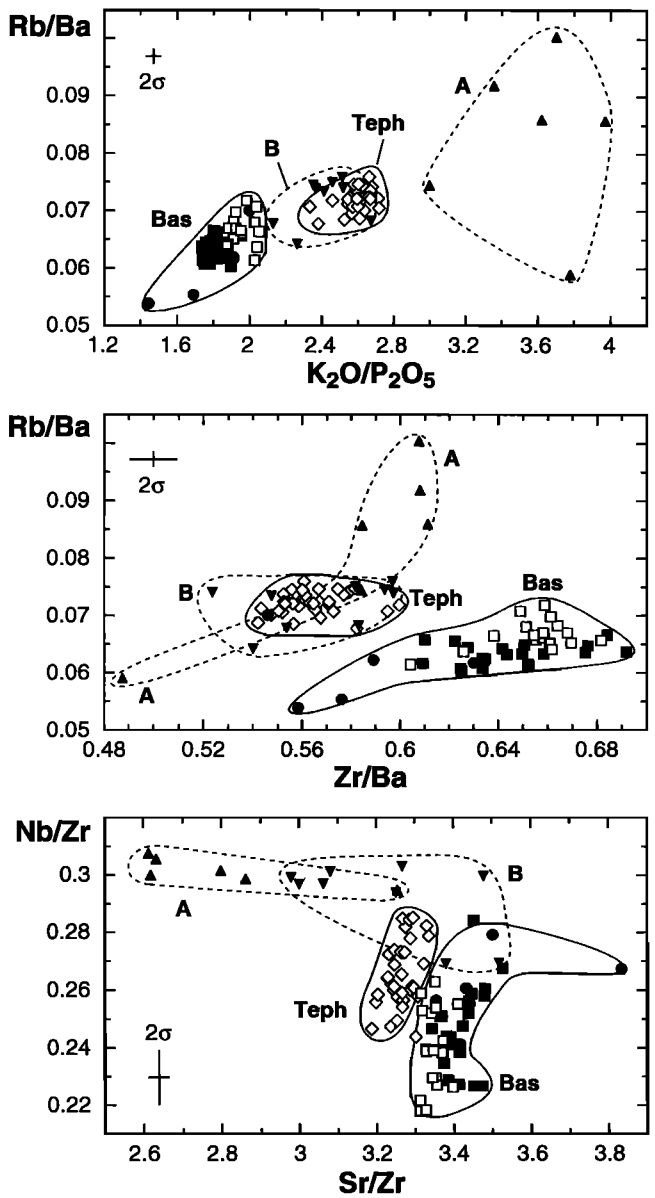

Figure 6c. Ratio plots of incompatible elements showing almost no overlap of the fields for the tephrite (Teph) and basanite (Bas) groups. The Hoyo Negro phonotephrites A and B form irregular fields with no apparent end-members and do not plot on a line with the tephrite or basanite groups. The late Duraznero basanites (shaded squares) plot intermediate between the Llano del Banco and Hoyo Negro basanites.

clinopyroxene and kaersutite is consistent with the depletion of the middle relative to the light and heavy REE and increasing La/Sm ratios from basanite to phonotephrite.

7.2. Relationship Between Tephrites and Basanites

The clearly distinct fields for the tephrite and basanite groups (Figures 5 and 6) suggest that the two magmas are not directly related to each other but represent distinct batches. Alternative hypotheses to produce the tephrite are (1) fractional crystallization and (2) mixing of basanite with an evolved magma or wall rock assimilation. Hypothesis 1 requires ~7 wt % of plagioclase or kaersutite in the fractionating assemblage, as shown by least squares mass balance for the major elements, and leaves large residuals for Sr and Ba (Table 4). Plagioclase fractionation is ruled out by the absence of negative Eu and Sr anomalies in all samples (Figure 8), by increase in CaO/Al_2O_3 and Sr with increasing SiO_2 (Figure 6), and by our barometry [cf. *Fisk et al.*, 1988]. Kaersutite fractionation would cause increasing Zr/Ba and decreasing K_2O/P_2O_5 from basanite to tephrite, opposite to what is observed (Figure 6c). Hypothesis 2 is unlikely because no evolved La Palma rock, including felsic xenoliths (our unpublished data, 1999), can produce the tephrite by mixing with the basanite (compare Figures 5 and 6b).

We further tested whether another historic La Palma basanite could have produced the 1949 tephrite by fractional crystallization. Surprisingly, mass balance calculations for these models yield generally better results than that for the 1949 basanite as a parent (sum of squared residuals (SSR) ≤ 0.01, using data from *Elliott* [1991] and Table 3; one model is shown in Table 4). Nevertheless, large residuals remain for Sr, Ba, and Zr (>100

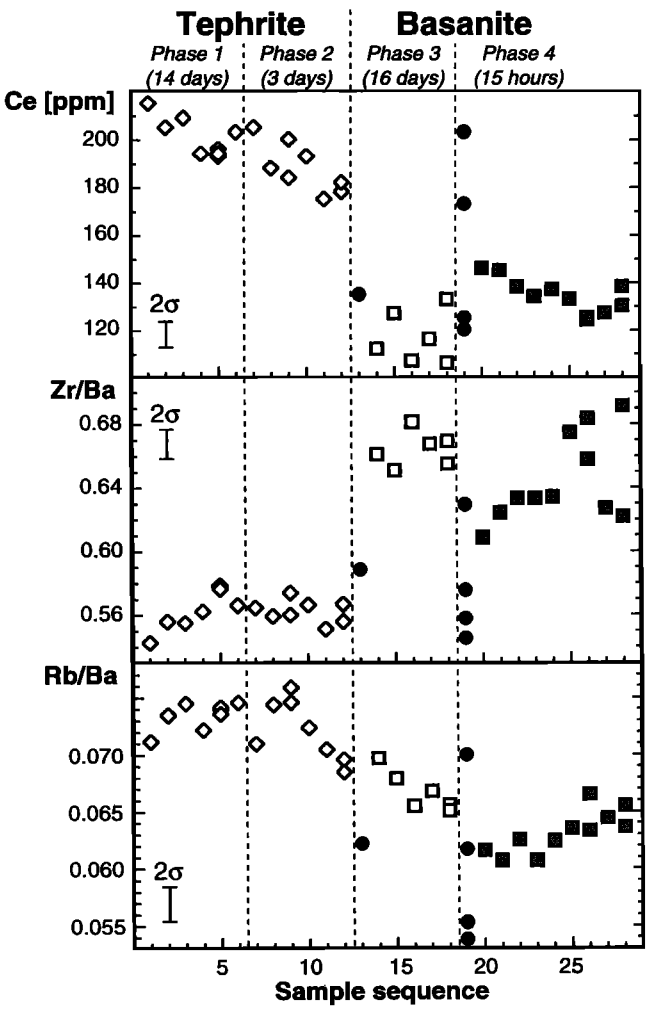

Figure 7. Systematic compositional variations of tephrites and basanites during the course of the eruption (error bars show 2σ analytical precision). The late Duraznero basanite from eruptive phase 4 (shaded squares) initially tends more to the Hoyo Negro (solid circles) and later to the Llano del Banco (open squares) basanite compositions. The diagram is based on 38 samples unequivocally representing a time series as based on field studies and the eruption chronology. Note that the sequence of samples shown is not linear in time (compare Figure 2).

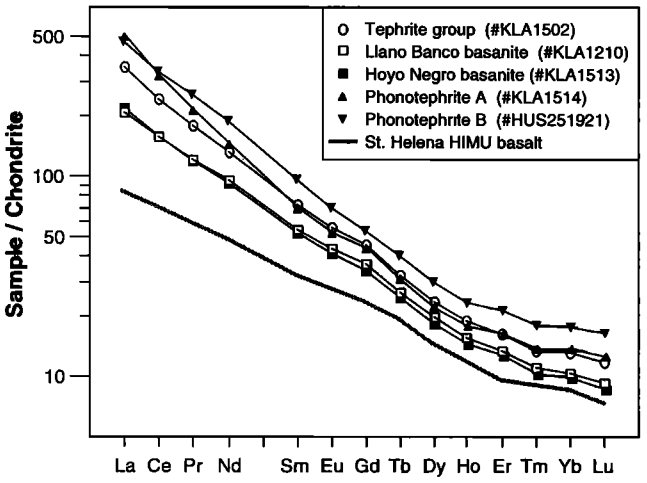

Figure 8a. Rare earth element (REE) element diagram of representative 1949 volcanics (ICP-MS data) normalized to average chondrite [*Boynton*, 1984]. The data for a primitive HIMU basalt from St. Helena island with 13.7 wt % MgO [*Chaffey et al.*, 1989] are shown for comparison (HIMU = high $^{238}U/^{204}Pb$). The concentrations increase from basanites to phonotephrites with strong enrichment of the light relative to the heavy REE ranging from 220 (basanites) to 290 (tephrites) and 380 (phonotephrites). The REE spectra are fairly smooth and have a mild concave upward shape becoming more pronounced in the evolved lavas.

ppm in most cases). Although there are uncertainties in the partition coefficients used, the large residuals do not indicate derivation of the tephrite from a historic basanite under closed-system conditions. Radiogenic isotopes do not resolve this question because all historic basanites from La Palma, as well as the 1949 tephrite, have identical Sr-Nd-Pb isotopic compositions within the analytical precision [*Elliott*, 1991; K. Hoernle, unpublished data, 1999].

We conclude that the tephrite and basanite groups represent two distinct magma batches that evolved and ascended separately and erupted subsequently. This scenario is consistent with very limited intermixing of the magmas despite low melt viscosities (~150 and 18 Pa s, respectively, as calculated after *Shaw* [1972]). The distinct compositions of the batches at least in part reflect source variations such as degree of melting [cf. *Elliott*, 1991], resulting in different silica activities and fractionation paths. The observed zonations within the tephrite and basanite batches (Figure 7) are consistent with compositional variations of the primary melts combined with incomplete homogenization after mixing events in the mantle.

The compositional differences between the basanites from the three eruptive centers are most easily explained by different degrees of melting (lowest for Hoyo Negro, highest for Llano del Banco) of a common source, likely with phlogopite in the residuum for all basanites to fractionate Rb/Ba and K_2O/P_2O_5. The Duraznero basanites have compositions intermediate between the Llano del Banco and Hoyo Negro basanites (Figure 6) and therefore could have been produced by (1) intermediate degrees of melting or (2) shallow mixing of the two end-members. The latter is consistent with mass balance calculations and could explain the Duraznero basanites initially tending more to the Hoyo Negro and later to the Llano del Banco compositions (Figure 7).

7.3. Melting Depths

The strong enrichment of the light and middle relative to the heavy REE of the 1949 and other Cumbre Vieja lavas (Figure 8) indicates residual garnet in the mantle source, which requires depths of melt extraction in excess of about 80 km if the source was garnet peridotite [e.g., *Hirschmann and Stolper*, 1996]. A comparison of the SiO_2 and FeO* contents of erupted lavas with contents predicted from dry melting experiments [*Hirose and Kushiro*, 1993] suggests melting depths of >100 km (3 GPa) if the magmas were derived from a lherzolite source (Figure 9). The possible presence of recycled oceanic crust in the form of pyroxenite in the source, however, as suggested by the HIMU-type trace element composition of the magmas, could significantly affect the SiO_2 and FeO* contents of the primary melts. Nevertheless, melting experiments on mixtures of peridotite and MORB [*Kogiso et al.*, 1998], which could represent recycled oceanic crust, also yield compositions that are consistent with melting depths of at least 80-100 km for the 1949 and other La Palma magmas (Figure 9), placing the source within or below the base of the lithosphere. The uniform Sr-Nd-Pb isotopic composition of all historic basanites [*Elliott*, 1991; K. Hoernle, unpublished data, 1999] suggests derivation from a common source.

7.4. Origin of the Hoyo Negro Phonotephrites

In most variation diagrams the Hoyo Negro phonotephrites A and B appear to represent mixing or crystal fractionation trends between the most extreme compositions combined with some contamination of the magmas as petrographically observed. In ratio plots of incompatible elements, however, these possibilities are ruled out because the former end-member compositions in Figures 5 and 6a do not form a trend but plot amid irregular fields (Figure 6c). The relationships shown in Figure 6 further indicate that neither group resembles a binary mixing line between the tephrite or basanite groups and evolved rocks from La Palma, such as phonolites and syenites. In addition, neither

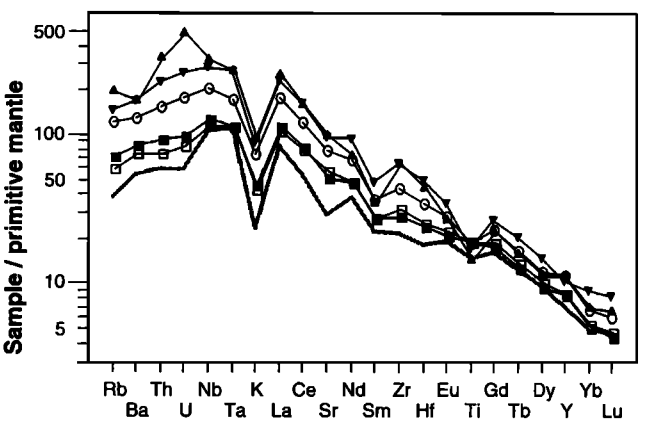

Figure 8b. Incompatible element diagram normalized to primitive mantle [*Hofmann*, 1988] (ICP-MS data except for Ti, K, Sr, and Zr). The data closely resemble the pattern from a St. Helena HIMU basalt [*Chaffey et al.*, 1989] characterized by a marked K trough and low Rb/Nb, Ba/Nb, and Ba/La ratios [*Weaver*, 1991]. The pronounced troughs for Ba, Sm, and Ti and the relatively high U/Th ratio of the most evolved phonotephrite A sample are consistent with kaersutite and apatite fractionation, whereas assimilation of 1 wt % of apatite can produce the relatively low U/Th ratio of the extreme phonotephrite B sample.

Table 4a. Results of Fractionation Calculations Based on Least Squares Mass Balance for Major Elements

	Model				
	Bas-Teph 1	Bas-Teph 2	Bas-Teph 3	Bas-Phon A	Bas-Phon B
Parent	Dur basanite KLA1507	Dur basanite KLA1507	1712 basanite KLA1624	HN basanite KLA1516	HN basanite KLA1516
Daughter	Dur tephrite KLA1502	Dur tephrite KLA1502	Dur tephrite KLA1502	Phonotephrite A WHJ9254	Phonotephrite B KLA1517
Fraction wt %					
Olivine	6.3	4.2	3.9	4.6	4.6
Clinopyroxene	18.2	15.1	18.3	15.8	16.0
Kaersutite	-	7.4	10.4	17.3	11.6
Plagioclase	6.6	-	-	-	-
Ti-magnetite	3.9	2.5	4.3	4.1	3.0
Apatite	-	-	0.7	0.4	-
Residual melt	64.9	70.8	62.4	57.9	64.9

	Bas-Teph 1		Bas-Teph 2		Bas-Teph 3		Bas-Phon A		Bas-Phon B	
	Calc	Resid	Calc	Resid	Calc	Resid	Calc	Resid	Calc	Resid
SiO_2	44.20	-0.05	44.13	-0.12	42.96	-0.01	43.44	0.10	43.44	0.10
TiO_2	3.35	-0.14	3.60	0.10	3.68	-0.19	3.64	-0.02	3.66	-0.04
Al_2O_3	13.77	0.01	13.49	-0.27	12.86	0.14	12.62	0.20	12.61	0.21
Fe_2O_3	13.76	0.02	13.58	-0.16	13.87	0.05	13.36	0.08	13.35	0.09
MnO	0.25	0.05	0.25	0.05	0.21	0.01	0.21	0.00	0.23	-0.02
MgO	8.04	0.00	7.98	-0.07	8.84	0.04	9.80	0.04	9.80	0.04
CaO	10.76	0.03	10.67	-0.05	11.57	0.06	10.96	0.01	10.96	0.01
Na_2O	3.78	-0.01	3.96	0.17	3.57	-0.04	3.56	-0.27	3.58	-0.29
K_2O	1.51	0.24	1.71	0.44	1.58	-0.04	1.70	-0.28	1.72	-0.30
P_2O_5	0.58	-0.14	0.65	-0.07	0.86	-0.03	0.69	0.15	0.59	0.25
SSR		0.10		0.36		0.07		0.23		0.30
Cr	36	0	63	27	36	0	51	-64	63	-64
Ni	17	-29	33	-13	18	-28	23	-54	39	-45
Rb	52	-4	47	-9	58	2	54	-16	49	-9
Sr	1202	-223	1241	-184	1625	179	1682	73	1636	18
Zr	405	-22	370	-57	469	42	553	4	502	7
Nb	119	0	108	-11	136	17	159	-5	144	-6
Ba	683	-103	616	-170	890	104	939	-1	850	1
La	100	-9	92	-17	145	36	152	-3	143	5
Ce	195	-20	177	-38	226	11	267	29	252	12
Nd	88	5	79	-4	90	7	108	24	103	16

Major elements in wt %; trace elements in ppm. Bas, basanite; Teph, tephrite; Phon, phonotephrite; Dur, Duraznero; HN, Hoyo Negro, SSR, sum of squared residuals; Calc, calculated; Resid, residual. See Table 3 for the compositions of parental and daughter magmas.

the tephrite nor the Llano del Banco or Duraznero basanites can have produced the phonotephrites by crystal fractionation because mass balance calculations using phenocryst and whole rock compositions yield poor results for major elements (SSR > 0.6) and high residuals for many trace elements (although increased concentrations of some incompatible trace elements such as REE, Zr, and Sr may partly reflect contamination as indicated by titanite xenocrysts in some Hoyo Negro rocks).

Mass balance calculations, however, show that the most primitive phonotephrite A and B compositions can be derived by crystal fractionation from relatively primitive Hoyo Negro basanites (Table 4; the relatively large Cr and Ni residuals most likely reflect crystal accumulation). These basanites are characterized by higher incompatible element concentrations and lower SiO_2 and Zr/Nb than the Llano del Banco and Duraznero basanites. Because of the restricted occurrence of phonotephrites at Hoyo Negro and because all of these rocks came from the same vent, it is likely that the primitive Hoyo Negro basanites are parental to phonotephrites A and B.

Table 4b. Partition Coefficients Used in Calculations

	Olivine	Clino-pyroxene	Kaersutite	Plagio-clase	Magnetite	Apatite
Cr	0.9	8	0.34	0	15	0
Ni	10	1.5	1.6	0	29	0
Rb	0	0.002	0.2	0.07	0	0
Sr	0	0.13	0.4...0.8	1.8	0	5.1
Zr	0	0.12	0.18	0.05	0.1	0.1
Nb	0	0.01	0.15	0.01	0.1	0
Ba	0	0.0002	0.4...0.8	0.23	0	0.7
La	0	0.06	0.17	0.19	0.003	6.8
Ce	0	0.1	0.26	0.11	0.003	6.1
Nd	0	0.2	0.44	0.09	0.003	5.4

Based on compilations from *Green* [1994] and on additional data for amphibole and apatite [*Irving and Price*, 1981; *Chazot et al*, 1996], olivine [*Beattie*, 1994], and clinopyroxene [*Skulski et al*, 1994; *Hart and Dunn*, 1993]. Where a range of coefficients is given, the values yielding the best solutions were used.

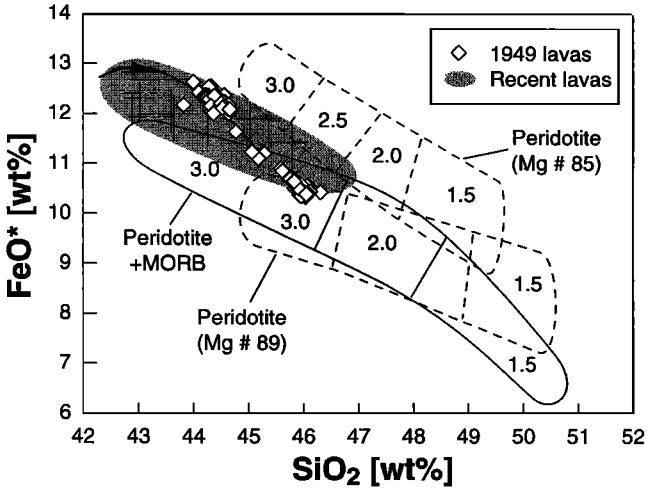

Figure 9. A plot of SiO_2 versus FeO* for the 1949 tephrite and basanite groups and other recent Cumbre Vieja lavas with MgO > 4 wt % compared to partial melts of possible source material suggests melting pressures above 2.5-3.0 GPa. Fields with dashed and solid lines encircle the range of dry partial melts of two relatively fertile peridotites [*Hirose and Kushiro*, 1993] and of mixtures of 50-67% peridotite with 33-50% MORB [*Kogiso et al.*, 1998]; numbers indicate experimental pressures in gigapascals. Thick line with arrow shows calculated path for olivine fractionation.

The compositional differences between phonotephrites A and B are interpreted to reflect different storage depths and fractionation paths. Calculated models show that the principal path for phonotephrite A includes kaersutite and apatite fractionation, which is consistent with decreasing P_2O_5 and concave upward REE patterns, high Rb/Ba ratios, and relative Ti depletion of the most evolved rocks (Figures 6 and 8), whereas the path for phonotephrite B includes olivine fractionation and possibly ~1% of apatite assimilation (apatite is common in cumulate xenoliths and as xenocryst inclusions). The more evolved phonotephrite A and B samples require contamination by wall rocks or phases such as titanite to explain their incompatible trace element contents. The higher kaersutite/olivine ratio of fractionating phases for phonotephrite A than phonotephrite B may indicate deeper fractionation levels and/or higher water contents, which is consistent with more degassing during ascent and more abundant reaction rims around kaersutites observed in phonotephrite A samples.

8. Discussion

8.1. Model of Ascent and Eruption of the 1949 Magmas

The simple model presented below illustrates the complexity of magma plumbing before and during the 1949 eruption. It is clearly not the only possible model and much of it is speculative due to lacking information; however, we believe that it is the simplest model consistent with the existing data and therefore serves as an end-member type model.

8.1.1. Storage and mixing in the mantle. After segregating from their source region the ascending magmas stagnated and differentiated to varying extents in reservoirs within the upper mantle. Mineral thermobarometry (Figure 4) indicates main fractionation levels at circa 600-800 MPa (20-26 km depth) and possibly also at 800-1100 MPa (26-36 km) which overlaps with the range indicated by CO_2-rich fluid inclusions for other Canary Island lavas [*Hansteen et al.*, 1998]. Magma transport in this depth range is governed by dikes formed by hydraulic fracturing [e.g., *Lister and Kerr*, 1991].

The evolution of the tephrite included mixing with a phonolitic magma as indicated by reversely zoned clinopyroxenes and kaersutites having euhedral to rounded cores with low Mg number. Magma mixing may have occurred in the inferred upper mantle reservoirs where the resulting tephrite subsequently resided. Likewise, the Llano del Banco and Duraznero basanites indicate at least two distinct mixing events because reversely zoned olivine and green-core clinopyroxene have strongly differing Mg number. We propose that an ascending magma batch containing Fo_{80} olivine and brownish clinopyroxene mixed with a relatively small volume of phonolitic magma at 600-800 MPa, producing green-core clinopyroxenes analogous to those in the tephrite. The resulting magma was later mixed with a relatively primitive melt producing Fo_{84} olivine as new phenocrysts (type 1) and as a rim around Fo_{80} olivine (type 2, Figure 3). This mixing event occurred a few months prior to eruption, as shown above by diffusion calculations.

Mixing of distinct magmas, including highly evolved melts, is common beneath La Palma, as reflected in the abundance of green-core clinopyroxenes in historic and prehistoric lavas studied by us and other workers [e.g., *Praegel*, 1986]. We visualize magma storage within the upper mantle occurring in a network of partly interconnected "pockets" from which magma batches are periodically expelled, similar to scenarios proposed for other alkalic basaltic provinces [*Duda and Schmincke*, 1985; *Dobosi and Fodor*, 1992]. This is consistent with our geochemical data, indicating that the tephrites and basanites were not in prolonged contact but evolved and ascended separately until surface activity began.

8.1.2. Ascent into the crust and filling of the rift system. The onset of weak, sporadic seismicity in 1936 [*Martel San Gil*, 1960] is interpreted to reflect the first batch of the 1949 magmas reaching the crust. Magma stagnation, accumulation, or lateral transport in the lower crust beneath La Palma is manifested by fluid inclusions in phenocrysts and xenoliths of the 1949 and other eruptions dominantly indicating pressures of 220-350 MPa, close to the Moho [*Klügel et al.*, 1997; *Hansteen et al.*, 1998] (Figure 4). We interpret this level as a major intrusion zone, possibly comprising a crystal-rich mush that may or may not solidify between successive magma batches, and apply the term "deep rift system".

We propose that low-degree, relatively primitive basanite entered the rift system beneath Hoyo Negro in 1936 and stagnated at three different levels, possibly within the crust (Figure 10a). Over the next 13 years, this basanite differentiated to form (1) phonotephrite B at the shallowest level, (2) phonotephrite A at an intermediate level, and (3) more evolved Hoyo Negro basanite at the deepest level; this reservoir was also the largest.

Beginning in February 1949, increasing magma pressure in the mantle reservoirs resulted in the propagation of dikes feeding tephrite from the mantle through the deep rift into the shallow rift system (Figure 10b). The magma probably stagnated at a level of neutral buoyancy at a few kilometers depth [*Ryan*, 1988; *Lister and Kerr*, 1991], which is consistent with fluid inclusion data [*Hansteen et al.*, 1998]. The "rift event" produced strong, shallow seismicity and ground cracking in southernmost La Palma during the 3 months prior to eruption [*Martel San Gil*, 1960], a period which coincides remarkably well with the last mixing event

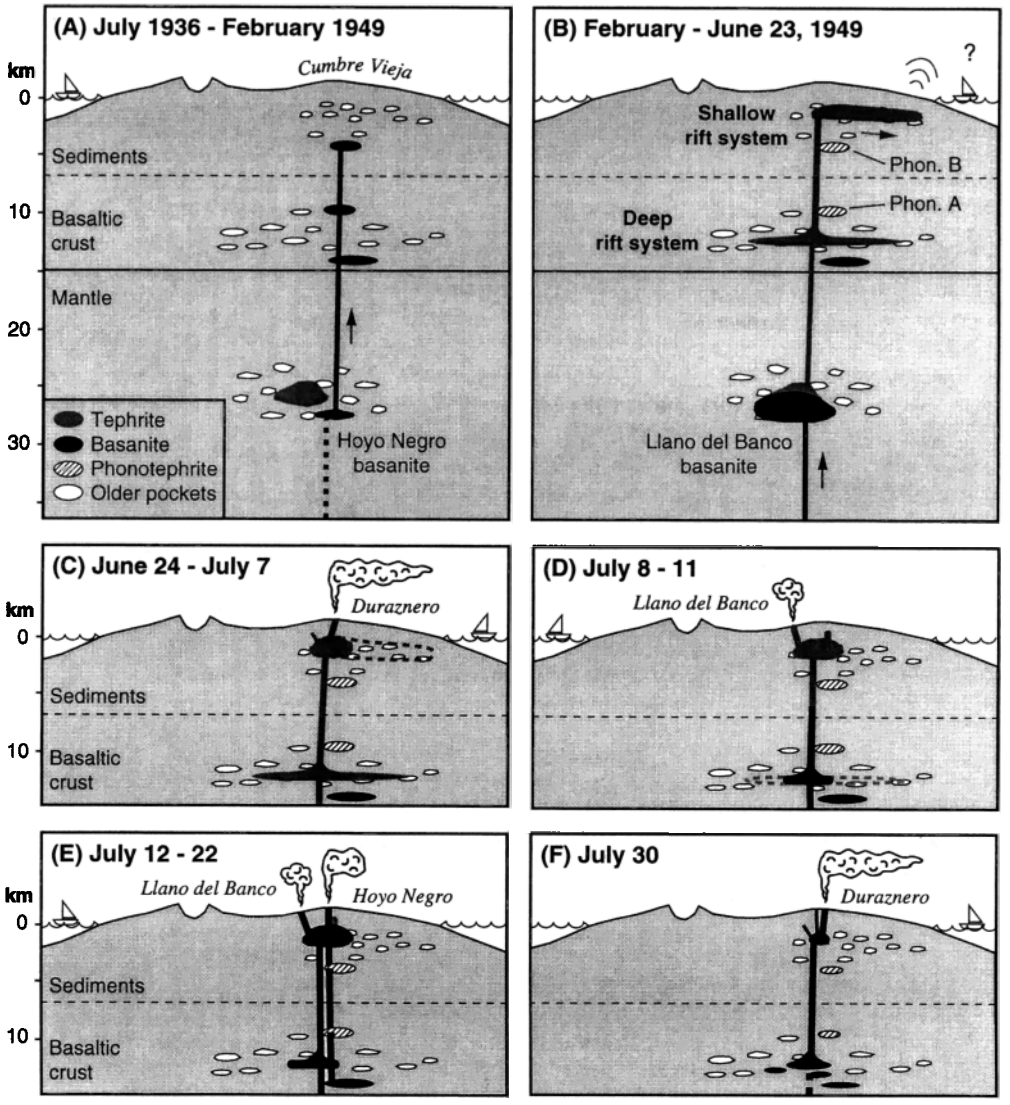

Figure 10. Schematic north-south cross section of La Palma illustrating our model of magma transport and storage during the 1949 eruption (note that three-dimensional relations cannot be well illustrated by the drawing; see text for details). Lithological boundaries are from *Ranero et al.* [1995]. (a) Between 1936 and 1949, low-degree basanite ascends from the upper mantle to the deep rift system beneath Hoyo Negro where it stagnates and differentiates at distinct levels, possibly within the crust. The basanite and tephrite group magmas reside and fractionate in the upper mantle. (b) At 3 months prior to eruption, following a mixing event in the mantle, basanitic magma pushes tephrite into the rift system to cause dike propagation and strong seismicity in southern La Palma. (c) In phase 1, Duraznero erupts tephrite and dikes propagate toward Llano del Banco. (d) In phase 2, Duraznero shuts down and Llano del Banco fissure erupts tephrite. The basanite follows the tephrite and erupts a few days later. (e) In phase 3, there is simultaneous eruption of basanite at Llano del Banco and basanite and phonotephrite at Hoyo Negro, which are closely linked through the rift system. (f) In phase 4, Duraznero erupts basanite of intermediate composition. Partial collapse of magma reservoirs produces abundant xenoliths that are carried to the surface.

inferred for the basanites from diffusion calculations. We thus propose that the dramatic increase in seismicity resulted from a sequence of events initiated by a mixing event in the mantle. The mixing produced the Llano del Banco basanite, which subsequently ascended, encountered the tephrite, and pushed it ahead; however, the rising magmas did not encounter the pockets of Hoyo Negro basanite and phonotephrites.

8.1.3. Eruption of the magmas. On June 24 a tephritic dike approached the surface at Duraznero and initiated phreatomagmatic explosions (phase 1, Figure 10c). Remarkably, the eruption occurred at the apex of the Cumbre Vieja, 10 km north of the locus of strongest seismic precursors and over 1000 m higher in elevation. Intense ground cracking north of Duraznero was presumably associated with shallow dike propagation along the rift [cf. *Rubin and Pollard*, 1987]. On July 8 a dike reached Llano del Banco (3 km to the north and 580 m lower in elevation), causing eruption of tephrite at increased rates and shutdown of Duraznero (phase 2, Figure 10d). Over the next 2 days, the gradual emptying of the tephrite reservoirs in the mantle was followed by the ascent of basanite along the tephrite conduits, which produced minor intermixing.

Facilitated by its lower viscosity, eruption of the basanite at

Llano del Banco induced further dike propagation and the opening of Hoyo Negro on July 12 (phase 3, Figure 10e). The apparently close hydraulic connection between Llano del Banco and Hoyo Negro most likely occurred along relatively shallow dikes [*Klügel et al.*, 1999], consistent with the development of a fault system between the vents [*Bonelli Rubio*, 1950; *Romero Ortiz*, 1951; *Carracedo et al.*, 1999]. Between July 12 and 22, some Llano del Banco basanite was erupted at Hoyo Negro, together with Hoyo Negro basanite and phonotephrite A and B, which presumably resided within the rift system as disconnected pockets alongside the main 1949 magma pathway. Such magma pockets can remain when parts of a storage system solidify between infrequent eruptions [*Wright and Fiske*, 1971; *Garcia et al.*, 1989; *Wright and Helz*, 1996]. Thus the Llano del Banco basanite either actively flushed the melts from these pockets to the surface at Hoyo Negro or triggered their rise. Incomplete mixing of the distinct batches and abundant schlieren in the Hoyo Negro rocks imply expulsion shortly after contact; in addition, the low eruption rate at this vent allowed preservation of such chemical heterogeneities.

The bulk of the erupted tephrite and basanite must have passed through the rift system quickly because clinopyroxene-melt barometry indicates mantle rather than crustal depths. Our diffusion calculations for the basanite indicate transfer times of hours to days, during which rapid degassing and crystallization caused the outermost rim zonation of olivine phenocrysts. The magmas did reside briefly in the lower crust, however, as shown by fluid inclusions in phenocrysts (Figure 4), which most likely reflects passage through the deep rift system.

As the activity at Llano del Banco began to decline, tholeiitic gabbro xenoliths began to appear in the lavas. After the activity ceased entirely for 3 days a final magma pulse re-activated Duraznero and Hoyo Negro on July 30 (phase 4, Figure 10f). The Duraznero basanite, intermediate in composition among the basanites, could either have been formed by intermediate degrees of melting or could reflect mixing of the Llano del Banco and Hoyo Negro end-members. We interpret the occurrence of crustal and mantle xenoliths almost exclusively in lava from the terminal phase of the eruption to reflect collapse of the plumbing system in the crust, and possibly the mantle, producing abundant fragments which were entrained into the rising magma [*Klügel et al.*, 1999].

8.1.4. Transport of mantle xenoliths. Remarkably, the Duraznero basanite and the peridotitic mantle xenoliths it carries have distinct ascent histories. The xenoliths indicate magma contact for tens of years and provide evidence for prolonged storage in the deep rift system [*Klügel*, 1998], whereas the basanite passed through the crust within hours to days. In

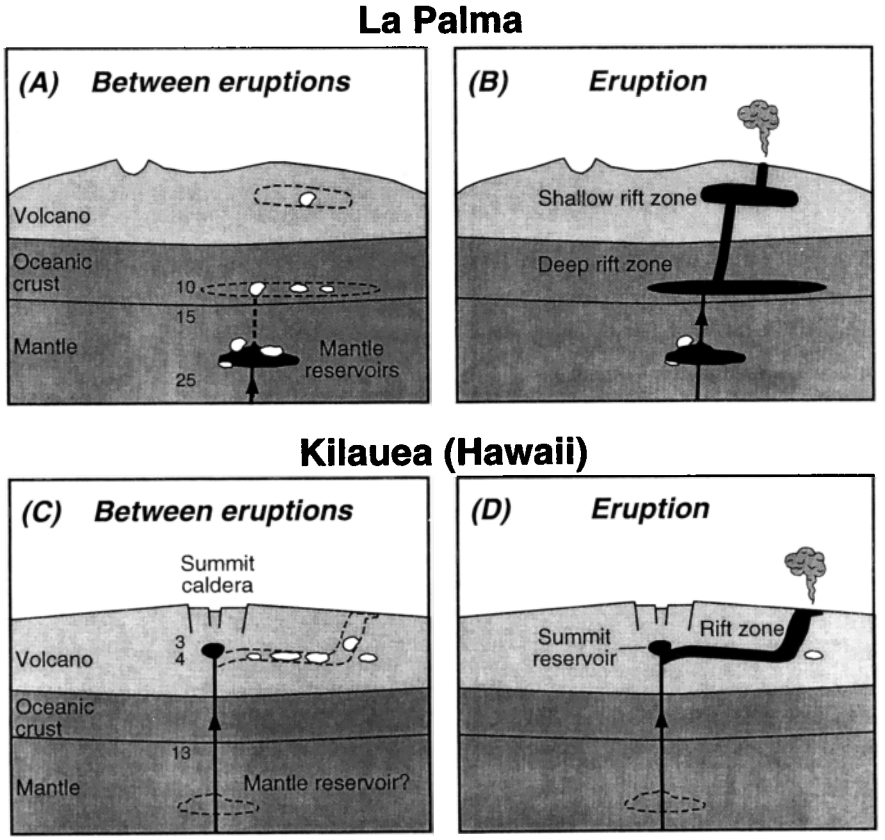

Figure 11. Simplified, schematic comparison of magma supply to Kilauea versus La Palma rift zone eruptions. Pockets with older, evolved magmas are shown in white; numbers indicate depths in km. The hypothetical cross section beneath Kilauea is after *Garcia et al.* [1996]. (a) Between La Palma eruptions, there is little or no magma fed into the volcanic edifice, which lacks a summit storage zone. (b) During La Palma eruptions, spaced tens to hundreds of years apart, magma is transported from mantle reservoirs through the deep and the shallow rift system toward the surface. It may encounter pockets of magma that has been stored and differentiated at different stages. (c) Between Kilauea eruptions, a continuous supply of sub-crustal magma enters the summit reservoir inflating the volcanic edifice [*Wright and Fiske*, 1971]. (d) During Kilauea eruptions, spaced years to tens of years apart, magma is fed from below and from the summit reservoir into the rift zone, where it mingles with magma that has been stored and slightly differentiated.

addition, the xenoliths are mantled by cumulate-like selvages containing kaersutite, which is not a phenocryst phase of the basanite. The xenoliths were thus transported from the mantle to the lower crust by earlier magma batches, some of which may be associated with the weak seismicity beginning in 1936. The earlier xenolith-bearing batches ponded in the deep rift system and produced a crystal mush in which the xenoliths were stored until, late in the 1949 eruption, conduit collapse spalled marginal debris into the basanite which then carried them to the surface. The minimum magma ascent rate of 0.2 m s^{-1} necessary to carry fist-sized peridotite xenoliths [*Klügel*, 1998] is consistent with the inferred transfer time through the crust.

8.2. Comparison With Kilauea Rift Zones

In contrast to the two rift zones of Kilauea (Hawaii), no collapse caldera is associated with the active Cumbre Vieja rift of La Palma, and there is no magma reservoir beneath the summit feeding the rift system (Figure 11). The absence of a summit reservoir on La Palma may reflect the longer periods between eruptions and the smaller volumes emitted per eruption than in Hawaii. Both of these features result from a much lower supply rate of basanitic magma to La Palma (eruptive rate 0.15-0.37 km^3 kyr^{-1} [*Ancochea et al.*, 1994] than of tholeiitic magma to Kilauea (10-100 km^3 kyr^{-1} [*Tilling and Dvorak*, 1993]). The net effect of the lower supply rates and absence of a summit reservoir is a storage system for La Palma in which only small and discontinuous pockets of residual magma can survive from one eruption to the next and in which pronounced fractionation is commonplace between eruptions, even though the bulk of the magmas (>90 vol %) is still basaltic.

For La Palma, compositionally bimodal or multimodal eruptions, involving distinct magma batches produced and evolved in the mantle and crust, are the norm. Kilauea rift zone eruptions, in contrast, commonly involve (1) magma accumulated in the summit reservoir, (2) pockets of magma stored along the rift, and (3) magma newly arrived from the mantle [*Wright and Fiske*, 1971; *Wright and Helz*, 1996; *Garcia et al.*, 1989] (Figure 11). Because the Kilauea system is almost continually supplied with new magma, geochemical differences among these three components are more subtle yet can be considerable in some cases. Not all erupted lavas pass through the summit reservoir, but mixing of distinct components within Kilauea's rift system is common [*Garcia et al.*, 1996]. This results in more gradual variations in the composition of the erupted lavas, whereas the relatively abrupt changes typical for La Palma imply minimal damping of compositional fluctuations and by inference smaller magma bodies within the rift system [*Albarède*, 1993].

It is inferred that significant mixing and lateral magma transport beneath Kilauea occur in the deeper parts of the rift system (3-10 km depth) consisting of more or less persistent magma bodies plus crystal mush [*Ryan*, 1988; *Garcia et al.*, 1989; *Delaney et al.*, 1990]. Xenolith and fluid inclusion studies indicate that La Palma has a deep rift system as well, albeit at 8-13 km depth within the oceanic crust [*Klügel et al.*, 1997; *Hansteen et al.*, 1998], which is consistent with tholeiitic MORB gabbros and ultramafic cumulates being the most abundant xenolith types. We cannot distinguish whether the deep rift beneath La Palma is a dike-like system, as proposed for Kilauea [*Delaney et al.*, 1990], or a system of sill-like bodies as supported by horizontal lithological boundaries in the lower crust [*Hill and Zucca*, 1987; *Lister and Kerr*, 1991]. The deeper parts of Kilauea's rift zones are overlain by the shallow rift system, which, as deduced by *Walker* [1987], comprise steeply dipping, subparallel dikes that serve as transient magma conduits and can propagate laterally for up to tens of kilometers [*Rubin and Pollard*, 1987]. The shallow rift system of La Palma probably has a similar structure, expressed by the alignment of vents, eruptive fissures, and cracks along the Cumbre Vieja ridge; however, the lateral extent of individual dikes appears to be significantly smaller than on Hawaii.

It is not known how the present rift system of La Palma formed or how it is related to the inferred lateral collapse of the western flank of the Cumbre Nueva at about 0.7 Ma, at which time activity shifted from the Taburiente shield in the north to the Cumbre Vieja rift zone in the south [*Navarro and Coello*, 1993; *Ancochea et al.*, 1994; *Carracedo et al.*, 1999]. We also have no constraints on whether the subcrustal conduits are located beneath the apex of the Cumbre Vieja or beneath the extinct Taburiente shield volcano. The latter would imply significant southward transport within the rift system and is supported by the southward shift of seismic foci of the 1949 precursors [*Klügel et al.*, 1999].

9. Conclusions

The 1949 eruption illustrates complex magma transport and storage systems beneath and within the Cumbre Vieja rift zone of La Palma. Common features of the 1949 and other recent La Palma eruptions include eruption of two or more distinct lava types, combined ridge and flank eruptions, abundant xenoliths in the late lavas, and long contact times between mantle xenoliths and magma [*Ibarrola*, 1974; *Hernandéz-Pacheco and Valls*, 1982; *Klügel et al.*, 1999]. Thus our proposed model of magma storage and transport may be applicable to other eruptions along the Cumbre Vieja rift.

The primary melts of La Palma magmas ascend from at least 80-100 km depth and indicate residual garnet, and possibly phlogopite, in the source. In addition to source variations such as degree of melting, the highly variable major and trace element composition of the erupted lavas is controlled chiefly by fractionation of olivine + clinopyroxene ± kaersutite ± Ti-magnetite at 600-800 MPa and probably 800-1100 MPa and by magma mixing. Mixing of mafic magmas with batches of highly evolved melts within the mantle is common, as indicated by reversely zoned phenocrysts such as green-core clinopyroxenes, yet results in relatively homogeneous whole rock compositions. Magmas without direct genetic links to each other ascend separately and are erupted together to produce strongly zoned eruptions. The volcanic rocks of the 1949 eruption reflect derivation from at least three distinct magma batches, all of which had a complex evolution involving mixing with distinct melts and shallow contamination.

Upon entering the crust, ascending magmas are temporarily stored and laterally transported in the deep rift system at 200-350 MPa, within the gabbroic oceanic crust, where cumulates form and dense xenoliths settle. Magma stagnation at this level is consistent with the common presence of tholeiitic MORB gabbro and ultramafic cumulate xenoliths, including plagioclase- and apatite-bearing cumulates and "immature" cumulates with interstitial glass and vesicles, all of which contain fluid inclusions indicating lower crustal pressures [*Hansteen et al.*, 1998]. When the rising magmas enter the shallow rift system at a few kilometers depth, propagating dikes produce intense seismicity until the eruption begins somewhere along the Cumbre Vieja ridge and its flank.

During a typical La Palma eruption, most of the erupted magma ascends from mantle depths and passes through the deep

and shallow rift system in a relatively short time, possibly hours to days. Some magma batches, especially those separated from the major conduits such as the Hoyo Negro basanite and phonotephrites, may become strongly contaminated by wall rock and pockets of older magmas that have been stored and differentiated within the rift system. Near the end of an eruption, partial collapse of the magma plumbing system produces fragments which are erupted as xenoliths within the terminal lavas.

In contrast to the rift zones of Kilauea volcano on Hawaii, La Palma lacks both a summit caldera and a summit reservoir feeding the Cumbre Vieja rift system. Both volcanoes are inferred to have their shallow rift zones underlain by a deeper part where some lateral magma transport and mixing occurs. The magma bodies in the deep rift system beneath La Palma are smaller and less persistent than those at Kilauea as reflected by a larger range in composition and more abrupt compositional changes during a single eruption. This coincides with a significantly lower rate of magma supply.

Appendix A: Analytical Methods

Whole rock analyses of major and trace elements were carried out on a Philips X'Unique X-ray spectrometer equipped with a Rh tube at Geomar in Kiel, using fused beads and pressed pellets. H_2O and CO_2 were analyzed on a Rosemount CSA 5003 infrared photometer. Trace elements of selected samples were analyzed by inductively coupled plasma mass spectrometry (ICP-MS) on a VG PlasmaQuad PQ1 at the Geologisch-Paläontologisches Institut, Christian-Albrechts-Universität in Kiel (see *Garbe-Schönberg* [1993] for details). Analytical precision (better than 5%) and accuracy were controlled by replicate analyses, blanks, and standards. In all figures the major element data have been normalized to 100 wt % on a H_2O- and CO_2-free basis.

Mineral and glass analyses were carried out on a Cameca SX-50 electron microprobe (EMP) at Geomar in Kiel. Analytical conditions included a beam current of 50 nA for olivine and 10 to 20 nA for other phases at an acceleration voltage of 15 kV. A focused beam was used for olivine, pyroxene, and oxides, and a rastered beam of 3x4 μm was used for all other phases. Counting times were 20 s on peak and 10 s on background. Some pyroxene analyses were carried out on a Jeol JXA 8900RL microprobe at the Institut für Geowissenschaften, Johannes Gutenberg-Universität in Mainz, using a defocused beam and peak counting times of 15 s.

Appendix B: Diffusion Calculations

By extrapolating the data of *Chakraborty* [1997] we use a constant interdiffusion coefficient D_{FeMg} for Fo_{80} olivine since the compositional dependence is weak within the range of interest (Fo_{74} to Fo_{84}). After correcting for oxygen fugacity by the relation $D_{FeMg} \sim (f_{O2})^{1/6}$ [*Buening and Buseck*, 1973], we obtain $D_{FeMg} = 1.3 \times 10^{-16}$ m^2 s^{-1} along the [001] direction of olivine for a model temperature $T = 1150$°C and $f_{O2} = 10^{-8}$ bar. Owing to the anisotropy of olivine, diffusion along [010] is slower than along [001] by a factor of ~4 [*Buening and Buseck*, 1973].

For olivine rims we use a simple one-dimensional diffusion model of an infinite halfspace with a planar interface toward the host melt because most type 1 olivines show a plateau of constant composition at their cores and because most zoning profiles were measured perpendicular to crystal faces. The boundary conditions are an initially constant olivine composition C_{core} and a constant interface composition C_{rim}. Following *Crank* [1975], the concentration C at a given time t and distance x is given by:

$$\frac{C - C_{rim}}{C_{core} - C_{rim}} = \mathrm{erf}\left(\frac{x}{2\sqrt{Dt}}\right) \quad \text{(B1)}$$

The diffusion time for a given profile length L is calculated by

$$t_{diff} = \frac{L^2}{16D} \quad \text{(B2)}$$

In order to place an upper limit on the time necessary to cause the reverse zonations of type 2 olivines the simplest diffusion model consists of a one-dimensional, initially heterogeneous olivine having a constant core composition C_{core} for $x > 0$ (Fo_{80}) and a constant maximum composition C_{max} for $x < 0$ (Fo_{84}). It is thus assumed that a concentration gradient exists a priori at $t = 0$, e.g. as a result of rapid growth of Fo_{84} olivine. The solution of this diffusion problem is provided by (B2) with L being half of the zonation length from core to maximum [*Crank*, 1975].

Acknowledgments. This work has benefited greatly from stimulating discussions with T. Hansteen and P. Sachs. We thank K. Wolff and A. Merkau for carrying out the XRF analyses, D. Garbe-Schönberg and T. Arpe for the ICP-MS analyses, and P. Glöer for technical assistance with the electron microprobe. Constructive reviews by M. Garcia, J. Stix, and D. Francis have significantly improved the manuscript. Our studies were supported by a stipend from the Studienstiftung des deutschen Volkes and a DFG fellowship (GRK 392/1-99) to A.K., by an Alexander von Humboldt fellowship to J.D.L.W., and by the Deutsche Forschungsgemeinschaft (DFG grants Sa 594/2-1 and Schm 250/47-1) and the National Science Foundation (NSF grant EAR-9105113 to K.H.). This work presents results of the Ph.D. thesis of A K

References

Abdel-Monem, A., N. D. Watkins, and P. W. Gast, Potassium-argon ages, volcanic stratigraphy, and geomagnetic polarity history of the Canary Islands: Tenerife, La Palma and Hierro, *Am. J. Sci.*, *272*, 805-825, 1972.

Albarède, F., Residence time analysis of geochemical fluctuations in volcanic series, *Geochim Cosmochim Acta*, *57*, 615-621, 1993.

Ancochea, A , F. Hernán, A. Cendrero, J. M. Cantagrel, J. M. Fúster, E. Ibarrola, and J Coello, Constructive and destructive episodes in the building of a young oceanic island, La Palma, Canary Islands, and genesis of the Caldera de Taburiente, *J. Volcanol Geotherm. Res.*, *60*, 243-262, 1994.

Beattie, P , Systematics and energetics of trace-element partitioning between olivine and silicate melts: Implications for the nature of mineral/melt partitioning, *Chem. Geol.*, *117*, 57-72, 1994.

Bonelli Rubio, J. M., Contribución al estudio de la erupción del volcan del Nambroque o San Juan (Isla de La Palma), 24 de Junio - 4 de Agosto de 1949, Talleres, pp. 5-22, Inst. Geogr. y Catastral, Madrid, 1950.

Boynton, W V., Geochemistry of the rare earth elements: meteorite studies, in *Rare Earth Element Geochemistry*, edited by P. Henderson, pp. 63-114, Elsevier Sci., New York, 1984.

Buening, D. K., and P. R. Buseck, Fe-Mg lattice diffusion in olivine, *J. Geophys. Res.*, *78*, 6852-6862, 1973.

Carmichael, I. S. E., and M. S. Ghiorso, The effect of oxygen fugacity on the redox state of natural liquids and their crystallizing phases, in *Modern methods of igneous petrology*, edited by J. Nicholls and J. K. Russell, *Mineral. Soc. of Am. Rev. Mineral.*, *24*, 191-212, 1990.

Carracedo, J. C., The Canary Islands: An example of structural control on the growth of large ocean-island volcanoes, *J. Volcanol. Geotherm. Res.*, *60*, 225-241, 1994.

Carracedo, J. C., S. J. Day, H. Guillou, and P. Gravestock, Later stages of volcanic evolution of La Palma, Canary Islands: Rift evolution, giant landslides, and the genesis of the Caldera de Taburiente, *Geol. Soc. Am. Bull.*, *111*, 755-768, 1999.

Chaffey, D. J., R A Cliff, and B. M. Wilson, Characterization of the St

Helena magma source, in *Magmatism in the Ocean Basins*, edited by A. D. Saunders and M. J. Norry, Geol. Soc. Spec. Publ., *42*, 257-276, 1989.

Chakraborty, S., Rates and mechanisms of Fe-Mg interdiffusion in olivine at 980°-1300°C, *J. Geophys. Res.*, *102*, 12,317-12,331, 1997.

Chazot, G., M. A. Menzies, and B. Harte, Determination of partition coefficients between apatite, clinopyroxene, amphibole, and melt in natural spinel lherzolites from Yemen; Implications for wet melting of the lithospheric mantle, *Geochim. Cosmochim. Acta*, *60*, 423-437, 1996.

Crank, J., *The Mathematics of Diffusion*, 414 pp., Oxford Univ. Press, New York, 1975.

Delaney, P T , R. S. Fiske, A Miklius, A. T. Okamura, and M. K. Sako, Deep magma body beneath the summit and rift zones of Kilauea volcano, Hawaii, *Science*, *247*, 1311-1316, 1990.

Dobosi, G , and R. V. Fodor, Magma fractionation, replenishment, and mixing as inferred from green-core clinopyroxenes in Pliocene basanite, southern Slovakia, *Lithos*, *28*, 133-150, 1992.

Duda, A., and H.-U. Schmincke, Polybaric differentiation of alkali basalt magmas· Evidence from green-core clinopyroxenes (Eifel, FRG), *Contrib. Mineral. Petrol.*, *91*, 340-353, 1985.

Duke, J. M., Distribution of the period four transition elements among olivine, calcic clinopyroxene and mafic silicate liquid: experimental results, *J. Petrol.*, *17*, 499-521, 1976.

Elliott, T. R., Element fractionation in the petrogenesis of ocean island basalts, Ph.D. thesis, The Open Univ., Milton Keynes, England, 1991.

Fisk, M. R., B. G J. Upton, C. E Ford, and W. M. White, Geochemical and experimental study of the genesis of magmas of Réunion Island, Indian Ocean, *J. Geophys. Res.*, *93*, 4933-4950, 1988.

Ford, C. E., D. G. Russell, J. A. Craven, and M. R. Fisk, Olivine-liquid equilibria: Temperature, pressure and composition dependence of the crystal/liquid cation partition coefficients for Mg, Fe^{2+}, Ca and Mn, *J. Petrol.*, *24* , 256-265, 1983.

Garbe-Schönberg, C. D., Simultaneous determination of thirty-seven trace elements in twenty-eight international rock standards by ICP-MS, *Geost. Newsl.*, *17*(1), 81-97, 1993.

Garcia, M. O., R. A. Ho, J. M. Rhodes, and E. W. Wolfe, Petrologic constraints on rift-zone processes; results from episode 1 of the Puu Oo eruption of Kilauea volcano, Hawaii, *Bull. Volcanol.*, *52*, 81-96, 1989.

Garcia, M. O., J. M. Rhodes, F. A. Trusdell, and A. J. Pietruszka, Petrology of lavas from the Puu Oo eruption of Kilauea volcano, III, The Kupaianaha episode (1986-1992), *Bull. Volcanol.*, *58*, 359-379, 1996.

Green, T. H., Experimental studies of trace-element partitioning applicable to igneous petrogenesis - Sedona 16 years later, *Chem. Geol.*, *117*, 1-36, 1994.

Hansteen, T. H., A. Klügel, and H -U. Schmincke, Multi-stage magma ascent beneath the Canary Islands: Evidence from fluid inclusions, *Contrib. Mineral. Petrol.*, *132*, 48-64, 1998.

Hart, S. R , and T. Dunn, Experimental cpx/melt partitioning of 24 trace elements, *Contrib. Mineral. Petrol.*, *113*, 1-8, 1993.

Hausen, H., Some contributions to the geology of La Palma, *Commun. Phys. Math. Finn. Acad. Sci.*, *35*, 1-140, 1969.

Hernandéz-Pacheco, A., and J. De la Nuez, Las extrusiones sálicas del Sur de la Isla de La Palma (Canarias), *Estud. Geol.*, *39*, 3-30, 1983.

Hernandéz-Pacheco, A., and M. C. Valls, The historic eruptions of La Palma Island (Canarias), *Arquipelago, Rev. Univ. Azores, Ser. C., Nat.*, *3*, 83-94, 1982.

Hill, D. P., and J. J. Zucca, Geophysical constraints on the structure of Kilauea and Mauna Loa volcanoes and some implications for seismomagmatic processes, in *Volcanism in Hawaii*, edited by R.W. Decker, T.W. Wright, and P.H. Stauffer, *U.S. Geol. Surv. Prof. Paper*, *1350*, 903-917, 1987.

Hirose, K., and I. Kushiro, Partial melting of dry peridotites at high pressures: Determination of compositions of melts segregated from peridotite using aggregates of diamond, *Earth Planet. Sci. Lett.*, *114*, 477-489, 1993

Hirschmann, M. M., and E M. Stolper, A possible role for garnet pyroxenite in the origin of the "garnet signature" in MORB, *Contrib. Mineral Petrol.*, *124*, 185-208, 1996.

Hoernle, K., Trace element and Sr-Nd-Pb isotopic geochemistry of Jurassic ocean crust beneath Gran Canaria (Canary Islands): Implications for the generation of OIB reservoirs and for crustal contamination of ascending OIB magmas, *J Petrol.*, *39*, 859-880, 1998.

Hofmann, A. W., Chemical differentiation of the Earth: The relationship between mantle, continental crust, and oceanic crust, *Earth Planet. Sci. Lett.*, *90*, 297-314, 1988.

Ibarrola, E., Temporal modification of the basaltic materials from 1971 eruption of the Teneguía volcano (La Palma, Canary Islands), *Estudios Geol., Vol. Teneguía*, 49-58, 1974.

Irving, A. J., and R. C. Price, Geochemistry and evolution of lherzolite-bearing phonolitic lavas from Nigeria, Australia, East Germany and New Zealand, *Geochim. Cosmochim. Acta*, *48*, 1309-1320, 1981.

Kaiser, C., The 1949 eruption of Volcan San Juan, La Palma, Canary Islands· Petrology and lava flow dynamics, diploma thesis, Univ. Bochum, Bochum, Germany, 1988.

Klitgord, K. D., and H. Schouten, Plate kinematics of the central Atlantic, in *The Geology of North America*, vol. M, *The Western North Atlantic Region*, edited by P. R. Vogt and B. E. Tucholke, pp. 351-378, Geol Soc of Am., Boulder, Colo., 1986.

Klügel, A., Reactions between mantle xenoliths and host magma beneath La Palma (Canary Islands)· Constraints on magma ascent rates and crustal reservoirs, *Contrib. Mineral. Petrol.*, *131*, 237-257, 1998.

Klügel, A., T. H. Hansteen, and H.-U. Schmincke, Rates of magma ascent and depths of magma reservoirs beneath La Palma (Canary Islands), *Terra Nova*, *9*, 117-121, 1997.

Klügel, A., H.-U. Schmincke, J. D. L. White, and K. A. Hoernle, Chronology and volcanology of the 1949 multi-vent rift-zone eruption on La Palma (Canary Islands), *J. Volcanol. Geotherm. Res.*, in press, 1999.

Kogiso, T., K. Hirose, and E. Takahashi, Melting experiments on homogeneous mixtures of peridotite and basalt: Application to the genesis of ocean island basalts, *Earth Planet. Sci. Lett.*, *162*, 45-61, 1998.

Le Maitre, R. W., P. Bateman, A. Dudek, J. Keller, M. J. Lameyre Le Bas, P. A. Sabine, R. Schmid, H. Sorensen, A. Streckeisen, A. R. Wooley, and B. Zanettin, *A Classification of Igneous Rocks and Glossary of Terms*, Blackwell, Malden, Mass., 1989.

Lister, J. R., and R. C. Kerr, Fluid-mechanical models of crack propagation and their application to magma transport in dykes, *J. Geophys. Res.*, *96*, 10,049-10,077, 1991.

Martel San Gil, M., *El Volcan de San Juan*, 239 pp., Talleres de Artes Gráficas, Madrid, 1960.

Middlemost, E. A. K., Evolution of La Palma, Canary archipelago, *Contrib. Mineral. Petrol.*, *36*, 33-48, 1972.

Navarro, J. M., and J. Coello, Sucesión de episodios en la evolución geológica de La Palma, mapa geológico de La Palma, Inst. Nac. para la Conserv. de la Nat., Madrid, 1993.

Olafsson, M., and D. H. Eggler, Phase relations of amphibole, amphibole-carbonate, and phlogopite-carbonate peridotite: Petrologic constraints on the asthenosphere, *Earth Planet. Sci. Lett.*, *64*, 305-315, 1983.

Pietruszka, A. J., and M. O. Garcia, The size and shape of Kilauea volcano's summit magma storage reservoir: A geochemical probe, *Earth Planet. Sci. Lett.*, *167*, 311-320, 1999.

Praegel, N. O., The petrology and geochemistry of Volcán Teneguía, La Palma, Canary Islands, Ph.D. thesis, Univ. of Copenhagen, Copenhagen, 1986

Putirka, K., Magma transport at Hawaii: Inferences based on igneous thermobarometry, *Geology*, *25* (1), 69-72, 1997.

Putirka, K., M. Johnson, R. Kinzler, J. Longhi, and D. Walker, Thermobarometry of mafic igneous rocks based on clinopyroxene-liquid equilibria, 0-30 kbar, *Contrib. Mineral. Petrol.*, *123*, 92-108, 1995.

Ranero, C. R., M. Torne, and E. Banda, Gravity and multichannel seismic reflection constraints on the lithospheric structure of the Canary Swell, *Mar. Geophys. Res.*, *17*, 519-534, 1995.

Roeder, P. L , and R. F. Emslie, Olivine-liquid equilibrium, *Contrib. Mineral. Petrol.*, *29*, 275-289, 1970.

Roeser, H. A , Magnetic anomalies in the magnetic quiet zone off Morocco, in *Geology of the Northwest African Continental Margin*, edited by U. Rad, K. Hinz, M. Sarnthein, and E. Seibold, pp. 61-68, Springer-Verlag, New York, 1982.

Romero Ortiz, J., La erupción del Nambroque en la isla de La Palma, *Bol. Inst. Geol. Min. Esp.*, *63*, 3-163, 1951.

Rubin, A. M., and D. Pollard, Origins of blade-like dikes in volcanic rift zones, in *Volcanism in Hawaii*, edited by R. W. Decker, T. W. Wright and P H. Stauffer, *U.S. Geol. Surv. Prof. Pap.*, *1350*, 1449-1470, 1987.

Rutherford, M. J., and P. M. Hill, Magma ascent rates from amphibole

breakdown: An experimental study applied to the 1980-1986 Mount St. Helens eruptions, *J. Geophys. Res.*, *98*, 19,667-19,685, 1993.

Ryan, M. P., The mechanics and three-dimensional internal structure of active magmatic systems: Kilauea volcano, Hawaii, *J. Geophys. Res.*, *93*, 4213-4248, 1988.

Schmincke, H.-U., Geology of the Canary Islands, in *Biogeography and Ecology of the Canary Islands*, edited by G. Kunkel, pp. 67-184, Junk BV, The Hague, Netherlands, 1976.

Schmincke, H.-U., Volcanic and chemical evolution of the Canary Islands, in *Geology of the Northwestern African Continental Margin*, edited by U. von Rad, K. Hinz, M. Sarnthein, and E. Seibold, pp. 3-20, Springer-Verlag, New York, 1982.

Schmincke, H.-U., A. Klügel, T. H. Hansteen, K. Hoernle, and P. v. d. Bogaard, Samples from the Jurassic ocean crust beneath Gran Canaria, La Palma and Lanzarote (Canary Islands), *Earth Planet. Sci. Lett.*, *163*, 343-360, 1998.

Shaw, H. R., Viscosities of magmatic silicate liquids: An empirical method of prediction, *Am. J. Sci.*, *272*, 870-893, 1972.

Skulski, T., W. Minarik, and E. B. Watson, High-pressure experimental trace-element partitioning between clinopyroxene and basaltic melts, *Chem. Geol.*, *117*, 127-148, 1994.

Sparks, R. S. J., and H. Pinkerton, Effect of degassing on rheology of basaltic lava, *Nature*, *276*, 385-386, 1978.

Staudigel, H., and H.-U. Schmincke, The Pliocene seamount series of La Palma/Canary Islands, *J. Geophys. Res.*, *89*, 11,195-11,215, 1984.

Takahashi, E., and I. Kushiro, Melting of a dry peridotite at high pressures and basalt magma genesis, *Am. Mineral.*, *68*, 859-879, 1983.

Tilling, R. I., and J. J. Dvorak, Anatomy of a basaltic volcano, *Nature*, *363*, 125-133, 1993.

Walker, G. P. L., The dike complex of Koolau volcano, Oahu: Internal structure of a Hawaiian rift zone, in *Volcanism in Hawaii*, edited by R.W. Decker, T.W. Wright, and P.H. Stauffer, *U.S. Geol. Surv. Prof. Pap.*, *1350*, 961-993, 1987.

Weaver, B. L., The origin of ocean island basalt end-member compositions: Trace element and isotopic constraints, *Earth Planet. Sci. Lett.*, *104*, 381-397, 1991.

White, J. D. L., and H.-U. Schmincke, Phreatomagmatic eruptive and depositional processes during the 1949 eruption on La Palma (Canary Islands), *J. Volcanol. Geotherm. Res.*, in press, 1999.

Wright, T. L., and R. S. Fiske, Origin of the differentiated and hybrid lavas of Kilauea volcano, Hawaii, *J. Petrol.*, *12*, 1-65, 1971.

Wright, T. L., and R. T. Helz, Differentiation and magma mixing on Kilauea's East Rift Zone: A further look at the eruptions of 1955 and 1960; 2, The 1960 lavas, *Bull. Volcanol.*, *57*, 602-630, 1996.

K. A. Hoernle and H.-U. Schmincke, Geomar Forschungszentrum, Wischhofstr. 1-3, D-24148 Kiel, Germany. (khoernle@geomar.de; hschmincke@geomar.de)

A. Klügel, Universität Bremen, Fachbereich Geowissenschaften, Postfach 330440, D-28334 Bremen, Germany. (akluegel@uni-bremen.de)

J. D. L. White, University of Otago, Geology Department, PO Box 56, Dunedin, New Zealand. (james.white@stonebow.otago.ac.nz)

(Received September 30, 1998; revised August 9, 1999;
accepted September 20, 1999.)